Probing and improving coherence in Free-electron lasers

Pop, Mihai

2022

Document Version:
Publisher's PDF, also known as Version of record

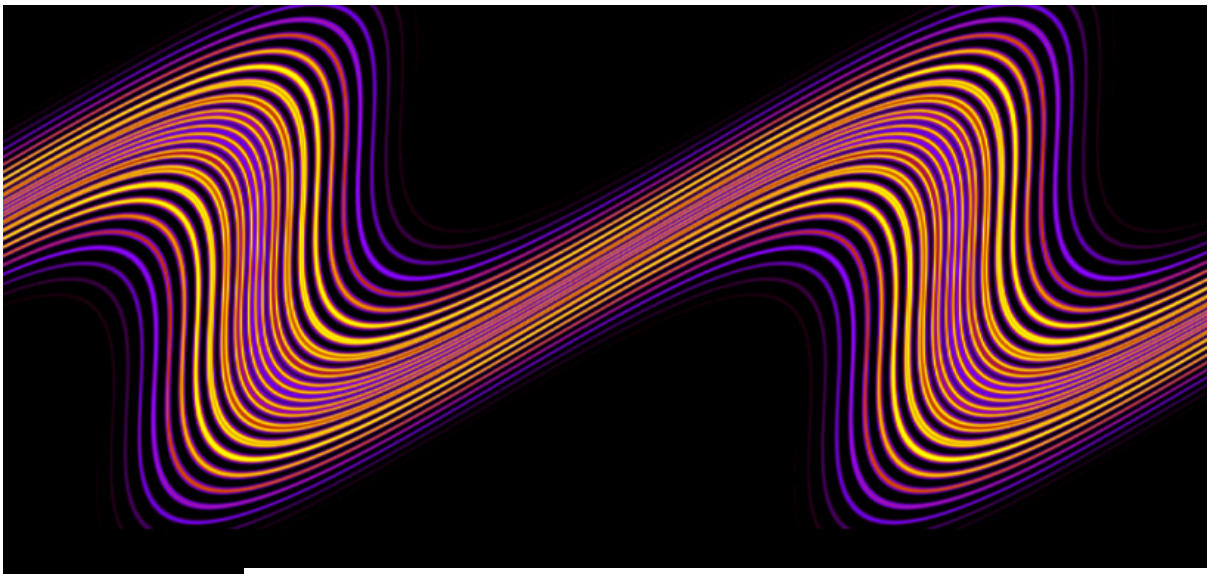

Probing and improving coherence in Free-electron lasers

MIHAI POP
DEPARTMENT OF PHYSICS | FACULTY OF SCIENCE | LUND UNIVERSITY

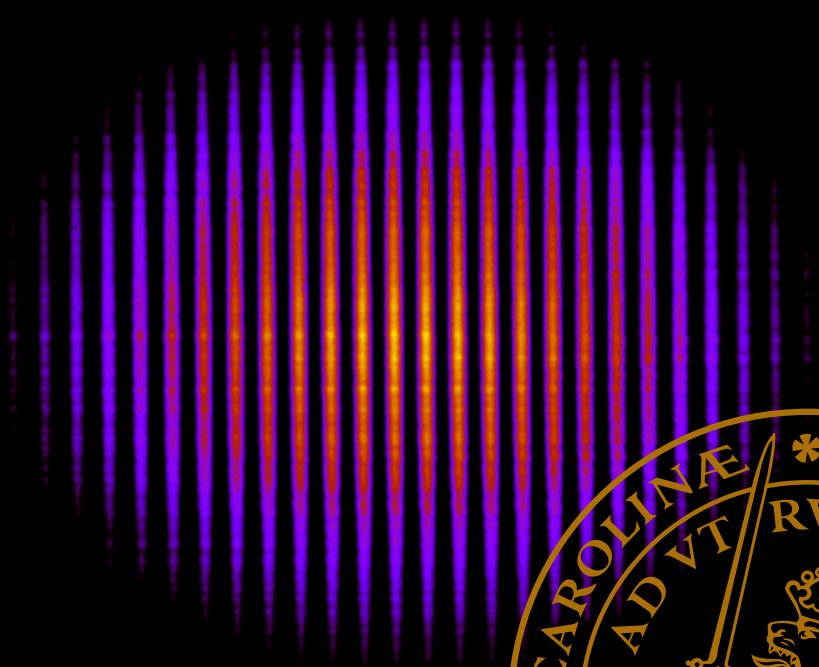

Probing and improving coherence in Free-electron lasers

Probing and improving coherence in Free-electron lasers

by Mihai Pop

LUND
UNIVERSITY

Thesis for the degree of Doctor of Phylosophy
Thesis advisors: Senior Lect. Francesca Curbis, Prof. Sverker Werin, Enrico Allaria PhD.
Faculty opponent: Prof. Atoosa Meseck

To be presented, with the permission of the Faculty of Science of Lund University, for public criticism at the Department of Physics (Rydbergsalen) on Wednesday, the 8th of June 2022 at 09:15.

Organization	Document name
LUND UNIVERSITY Department of Physics Box 124 SE–221 00 LUND Sweden	**PhD Thesis**
	Date of disputation 2022-06-08
	Sponsoring organization
Author(s) Mihai Pop	

Title and subtitle

Probing and improving coherence in Free-electron lasers

Abstract

Free electron lasers or FELs, have transformed the way science has been done in the last decades by providing coherent, highly brilliant radiation at wavelengths not achievable with conventional lasers. Their most important characteristic, along side brightness, is their coherence, which allows users to perform experiments that rely on precise phase characteristics of the probing radiation.

The FEL generates intense radiation by transferring energy from a relativistic electron beam to the EM field. Both the electron beam properties and the FEL-process itself determine the final characteristics of the FEL radiation. Through specific numerical and experimental tools it is possible to probe the coherence properties of FELs and gain insight into the fundamental processes influencing them. By understanding these processes, we can improve the coherence of the resulting FEL radiation using optical lasers or magnetic elements to act on specific features of the electron beam.

Investigations of transverse coherence by a Young-like experimental setup revealed differences between SASE and seeded FELs in the way that coherence is built up during the amplification process. Using the existing formalism, we used a double slit experiment to determine the transverse coherence of an FEL at various stages in the amplification process in both seeded and SASE operation. The results revealed significant differences in the way coherence is built up in the two FEL operation modes.

Longitudinal coherence improvement by EEHG seeding requires a strong magnetic chicane, which can makes it vulnerable to collective instabilities in the electron beam. This work shows how one can mitigate the effect of these instabilities by a creating a wavelength dependence with time of the seed laser. The EEHG technique is also explored here as a seeding option for SXL, the soft X-ray FEL at MAX IV.

Key words

Free electron laser, lightsource, synchrotron radiation, coherence, double-slit, simulations, EEHG, SASE, Seeded, HGHG

Classification system and/or index terms (if any)

Supplementary bibliographical information		Language English
ISSN and key title		ISBN 978-91-8039-266-2 (print) 978-91-8039-265-5 (pdf)
Recipient's notes	Number of pages 144	Price
	Security classification	

Signature 

Date 2022-05-10

Probing and improving coherence in Free-electron lasers

by Mihai Pop

LUND
UNIVERSITY

Cover illustration front: Longitudinal phase space of EEHG seeded electron beam and Interference pattern from double slit coherence measurement

Cover illustration back: Transverse and longitudinal coherence in a light beam by *Mahsa Pezhman*

Funding information:

Department of Physics, Faculty of Science, Lund University, Sweden

ISBN: 978-91-8039-266-2 (print)
ISBN: 978-91-8039-265-5 (pdf)

Printed in Sweden by Media-Tryck, Lund University, Lund 2022

Media-Tryck is a Nordic Swan Ecolabel certified provider of printed material. Read more about our environmental work at www.mediatryck.lu.se

MADE IN SWEDEN

Dedicated to my loving wife,
Irina

Contents

List of publications

This thesis is based on the following publications, referred to by their Roman numerals:

I **Considerations on implementing EEHG with a strong linear chirp**

M. Pop, F. Curbis, S. Werin, W. Qin
Proceedings of 39th Free Electron Laser Conference, 2019, pp. 262–265, Publisher: JACOW

II **A peak finding algorithm for FEL spectra characterization**

M. Pop, E. Allaria, F. Curbis
Proceedings of 39th Free Electron Laser Conference, 2019, pp. 388–391, Publisher: JACOW

III **Single-shot transverse coherence in seeded and unseeded free-electron lasers: A comparison**
M. Pop, E. Allaria, F. Curbis, et al.
Physical Review Accelerators and Beams, published 6th April 2022 DOI:10.1103/PhysRevAccelBeams.25.040701

IV **Mitigation of CSR induced spectral broadening in EEHG FEL**

M. Pop, F. Curbis, S. Werin, E. Allaria
Manuscript

V **Analysis of the effect of energy chirp in implementing EEHG at SXL**

M. Pop, F. Curbis, B.S. Kyle, S. Pirani, W. Qin S. Werin
Proceedings of the 12th International Particle Accelerator Conference, 2021 pp. 1566–1569, Publisher: JACOW

VI **Discussion on CSR instability in EEHG Simulation**

D. Samoilenco, W. Hillert, F. Curbis, **M.Pop**, S. Werin, P. Niknejadi, G. Paraskaki and F. Panek
Proceedings of the 12th International Particle Accelerator Conference, 2021 pp. 1622–1625, Publisher: JACOW

Publications I participated in but are not included in this thesis

Coherent soft X-ray pulses from an echo-enabled harmonic generation free-electron laser
P. Rebernik Ribič et al.
Nature Photonics doi:10.1038/s41566-019-0427-1
This important work published in Nature Photonics has for the first time experimentally demonstrated the possibility for the EEG seeding scheme to generate highly coherent pulses down to the soft X-ray wavelength range. I contributed to the work during the experiment participating to one of the measurement sessions in July 2018. I have been also involved in the data analysis and simulations.

The FEL in the SXL project at MAX IV

Weilun Qin, Francesca Curbis, Joel Andersson, Vitaliy Goryashko, Lennart Isaksson, Billy Kyle, Filip Lindau, Erik Mansten, **Mihai Pop**, Peter Salén, Hamed Tarawneh, Pedro F. Tavares, Sara Thorin, Alexey Vorozhtsov, Sverker Werin
doi:10.1107/S1600577521003465
A paper describing the key features of the soft Xray FEL envisioned at MAX IV. I contributed to the simulation work.

Flexible ptychography platform to expand the potential of imaging at free electron lasers
Konstantin Kharitonov, Masoud Mehrjoo, Mabel Ruiz-Lopez, Barbara Keitel, Svea Kreis, Martin Seyrich, **Mihai Pop**, Elke Plönjes
Optics Express doi:10.1364/*oe*.426931
A paper which describes a special ptychography reconstruction method that is able to retrieve both the sample and the probing EM radiation. As my first encounter with the topic I participated in the data acquisition during the experiment.

Acknowledgements

This Thesis is the culmination of 4 and a half years of work which would have been aimless, poorly executed and lacking in intensity without the help, guidance and support of numerous people whom I would like to mention here. First and foremost I would like to thank my supervisor Francesca Curbis who, alongside my co-supervisor, Sverker Werin, provided constant support and helped me create structure in my ideas. I could not have gone through my PhD studies without your guidance. I would also like to thank my co-supervisor from Italy, Enrico Allaria, who provided me with the opportunity to work on several exciting projects and who was always available for discussions and questions. A huge "thank you!" goes out to Giovanni De Ninno whose knowledge, tenacity and constant support were instrumental in helping me publish my first paper.

Next I would like to thank Weilun Qin and Saeid Pirani, colleagues in our group during my time here, and who have helped me understand difficult topics and selflessly took time to aid me in my work. A debt of gratitude is owed to the staff and personnel at MAX IV for providing help in using the computing infrastructure and to the division of synchrotron radiation for providing a great working environment. A special thank you goes to the staff at FERMI FEL for making me feel welcomed during my three work-visits at the facility.

For opening the doors of Physics to me, I would like to thank my high-school teacher Mihaela Leşe and my Bachelor degree supervisor Daniel Andreica, you shaped me to think like a physicist.

None of this would have been possible without my loving parents who nurtured me and who allowed me to soar in my pursuit of knowledge. Knowing I could always count on them to be there for me enabled me to dream big. I would now like to show my gratitude to all my family and friends who maybe do not get mentioned by name but who filled me with joy and hope every time I would see them. To my brother whom I love very much and who remained closer to home, maybe in some small part because his older brother had the crazy idea of studying in Sweden. To my family in Cluj, for making my time studying in Cluj, away from home feel easier, they hold a special place in my hart. To my best friend Claudiu Bulbucan, who has been climbing this steep mountain of becoming a physicist with me for almost 12 years. He and his wife Delia, were ideal conversation partners, helping me sharpen my mind during all this time. I thank my friends Payam Shayesteh and Mahsa Pezhman for welcoming me to the neighbourhood in which I wrote most this thesis. And of course, to my wife and love of 14 years, Irina, for her unselfish support throughout this journey, I could never thank you enough for what you have given me.

Popular science description

The tools by which scientists investigate the world are numerous and quite diverse. One of the most common tools is, without a doubt **light**. The uses of light as an investigation tool, range from telling when a fruit is ripe, by its color, to pinpointing our position on the globe by detecting light bouncing from satellites. We rely on light for X-ray medical investigation and for the biometric data the our smart watches collect.

Almost all experiments using light involve three steps: 1. creating a ”good” beam of light; 2. directing that light towards the thing we want to investigate (our object); 3. measure the light bouncing of our object. The key to a good measurement starts with a good beam of light. This work deals with the first step, how to make and how to tell if you have made a ”good” light beam.

To help visualize the light beam, it can be useful to imagine it as an elongated ball of water. Lets assume we want to use it to measure the temperature of an object. We produce the water ball at a certain temperature, hit the object with it and then measure the temperature of the water droplets splashing away from the object. If the object is hotter than the water, our droplets will have a higher temperature after hitting the object or, if the object is colder, the droplets will have a lower temperature.

It is possible that the water does not have the same temperature everywhere, perhaps the center is warmer than the outsides or maybe the zones with hot and cold water are randomly placed throughout the ball. In this case, it will prove difficult to estimate the temperature of the object since there are a lot of possible temperatures the water droplets can have even before hitting the hot/cold object. We would, therefore, like to have a uniform temperature all through the water ball. Similarly, investigating objects with light requires that it is uniform, therefore, in this thesis we focus on ways of telling how uniform any beam of light is.

Assume that we had, in a jar, a substance which glows red when you shine blue light on it, but the jar broke and it scattered the substance all over the floor. It would be simple to find the substance if we had a flash-light that emits only blue light, we would start the flash-light and collect the substance which appeared red. However, if our flash-light produces both blue and red light, other things may appear red and therefore we would not know where our substance really is. The color of the light is one of the properties we want to keep uniform throughout the beam.

A free-electron laser (FEL) is a lightsource that produces light beams of effectively a single color. As its name suggests, it is a special kind of laser that uses moving electrons to produce light. It is more intense than ”regular” lasers so, some researchers prefer

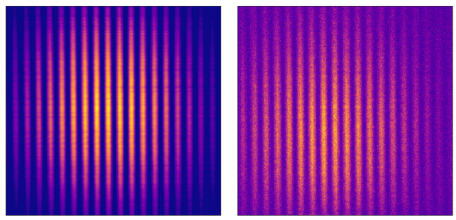

Figure 1: Examples of interaction between coherent (left) and incoherent (right) parts of the light beam

it over ”conventional” sources because experiments that would take days to complete with these other sources take just hours when using a FEL.

The work presented in this thesis focuses on measuring how uniform, or *coherent*, a light beam from a FEL is and how to make it more uniform. To measure how *coherent* (or uniform) two parts of the same beam are, you simply have to make them interact with each other. This is done by placing a mask in front of the beam so that only light from the two regions of interest passes through. If the interaction produces ”clean” patterns, it is a good indication that these two parts are coherent with each other.

This can be understood by thinking of two violins playing together. Perhaps you cannot tell if any one of them is out of tune, but if you play them together, you can determine if they are in-tune with each other. If the two try to play the same note and a clear sound is produced, it means they are in-tune, *coherent*; however, should they be even slightly out of tune, the sound will become distorted and ”noisy”.

In figure 1 we have two examples of interaction, one from a *coherent* and one from a less *coherent* light beam. Can you tell which is which? if you guessed that the one on the left side was more *coherent*, congratulations, you now know how to tell if a light beam is *coherent* or not.

In order to improve the coherence in FELs we first have to see how they emit light. In a FEL a large number (10 billion) of fast traveling electrons are made wiggle by placing magnets close to their paths, this ”wiggling” makes the electron emit light. The position of the electrons relative to each other determines how *coherent* the light beam will be. If the electrons are ordered properly, the light will also have smooth, uniform properties.

The key, then, to nice, *coherent* light beams lies with the electrons that produce them. The electron bunch can be made more orderly by using magnets and ”conventional” lasers to move electrons around. In this work we show that the coherence of the resulting radiation can be further improved if one uses a laser, whose color depends on time, to move the electrons more accurately within the electron bunch.

Probing and improving coherence in Free-electron lasers

Chapter 1

Introduction

Since its conceptualization in 1971[1], the Free Electron Laser (FEL) has captured the interest of researchers around the world as it promises extremely brilliant light pulses with tunable wavelength. Unlike optical lasers[2], FELs[3,4] use free electrons, accelerated to relativistic velocities, to generate synchrotron radiation with "laser-like" properties[5,6,7].

A schematic layout of a general FEL is presented in figure 1.1. The electrons are created in an electron gun and are then accelerated by a linear accelerator (LINAC),typically to energies of a few GeV. To reach the high current required for the FEL process, bunch compressors are used. Electrons and radiation interact in periodic magnetic structures called undulators where energy is transferred from the electrons to the radiating field.

At the end of the undulator section, the electrons are dumped and the light, after passing through some optical elements, finally reaches the experiment station. The highly brilliant light produced by FELs has enabled researchers to probe, with a single pulse, phenomena at the nanometer scale and within time frames of a few femtoseconds[8]. Users at FEL facilities can reduce the time required to perform an experiment by orders of magnitude. In table 1.1 there is a list of existing FEL facilities, in the soft and hard X-ray regimes, and their operational parameters.

As more and more experiments require high degrees of longitudinal and transverse coherence[9,10], there is a need to improve these properties in FELs. Although *coherence* is a quite "general" word used in almost all branches of physics, here it is used in reference to electromagnetic (EM) radiation. We can think of coherence as a property of two regions in the EM field that tells us how "similar" these two regions are in terms of amplitude and phase.

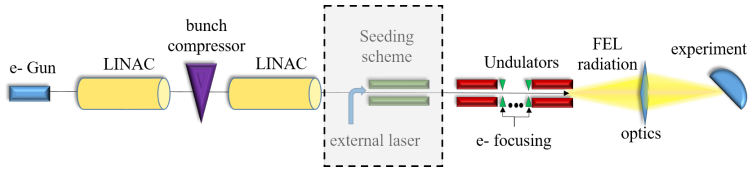

Figure 1.1: Layout of a typical FEL facility, from electron gun to experiment.

The most common type of FEL relies on a process called self amplified spontaneous emission (SASE)[3,4] to generate high intensity radiation. In this type of FEL, electrons interact with the radiation they produce themselves in a long undulator line (figure 1.1 without the "seeding scheme" and "external laser" in). This process however is intrinsically stochastic and, as a result, its longitudinal coherence is far from the one of conventional lasers, but the radiation is still considered narrow band, i.e., $\Delta\omega/\omega \approx 10^{-3}$.

A widely used method of improving longitudinal coherence has been to "seed" the electron beam by creating long distance order between the electrons (figure 1.1 with seeding scheme). Various seeding concepts[11,12,13,14] have been proposed, but each innovative scheme comes with its own challenges that need to be addressed.

G. Stupakov proposed in 2008[14] and demonstrated, with his colleagues, in 2009[15] a seeding scheme called Echo Enabled Harmonic Generation (EEHG), which can create significant bunching at harmonics as high as 100 of a conventional seed laser[16,17,18].

The soft X-ray FEL proposed to be built at MAX IV, called SXL[19], could also benefit from a coherence enhancement seeding option such as EEHG. After initial work describing the effect of electron energy chirp in EEHG FELs (**paper I**), I contributed to the conceptual design report of a SXL by designing a suitable EEHG seeding section. The strong residual energy chirp present at SXL poses unique challenges that were addressed in the EEHG seeding proposal presented in **paper V**.

One of the most important elements in an EEHG lattice is a strong dispersive section that moves electrons w.r.t. each other, creating extremely fine structures in the longitudinal phase space of the electron beam. However, this element is subject to the detrimental effect of Coherent Synchrotron Radiation (CSR) which is especially harmful for EEHG, given the complex phase space distribution it creates. By tailoring the wavelength profile of a seed laser, I show that it is possible to mitigate the CSR effect and improve by 50 % the longitudinal coherence of the FEL radiation. A full study on this topic is presented in **paper IV**.

Table 1.1: Examples of existing (or under construction) X-ray FEL facilities around the world

Name (Country)	$\lambda_{rad}[nm]$	Electron energy [GeV]	Photon flux $[photons/s]$
Hard X-ray			
LCLS (US)	$0.1 - 4.3$	14.3	10^{13}
EuXFEL (Germany)	$0.05 - 4.7$	17.5	10^{12}
PAL XFEL (S.Korea)	$0.08 - 6$	10	10^{12}
SHINE (China)	$0.05 - 3$	8	$-$
SACLA (Japan)	$0.06 - 0.3$	8.5	$4 \cdot 10^{11}$
SwissFEL (Switzerland)	$0.1 - 7$	5.9	$1 \cdot 10^{12}$
Soft X-ray			
FLASH (Germany)	$4 - 45$	1.2	$3 \cdot 10^{33}$
FERMI (Italy)	$7 - 65$	1.3	10^{13}
SXFEL (China)	$1.2 - 12$	1.6	10^{13}

As part of the work to detect effects that ruin longitudinal coherence, I present in **paper II**, a tool developed to detect modulations in the electron beam, by their effect on the FEL spectra. This numerical analysis tool can infer the electron density modulation wavelength by finding periodic side-bands in the FEL spectra.

On the other hand, transverse coherence seems to be intrinsically high for both SASE and seeded FELs[20,21,22], and studying the process by which it builds up can shed new light on this fundamental property. For this purpose, we used the capability of the FERMI FEL, to investigate the transverse coherence in both SASE and seeded configurations. The work, fully presented in **paper III**, shows that, in the same machine, SASE and seeded FEL reach similar degrees of transverse coherence. However, this property seems to develop through different mechanisms for the two modes of operation.

This work summarizes my efforts to improve the understanding of the coherence properties in FELs. **Chapter 2** gives the reader some theoretical notions about FELs, focusing on the SASE and seeded modes of operation to contextualize the work presented in the attached papers. **Chapter 3** details the framework of statistical coherence and describes how the coherence of FEL radiation is expressed by a few statistical functions. The methods used throughout the papers are described in **chapter 4** and range from directly analyzing experimental data, to numerical simulations and theoretical analysis. A comparison of the transverse coherence properties is carried out in **chapter 5** while **chapter 6** looks more in-depth at implementing the EEHG seeding option in a FEL. The thesis concludes with a summary of the work presented and suggests new avenues that might be explored in the future.

Chapter 2

FEL theory

Free-electron lasers rely on the exchange of energy between a relativistic electron beam and an electromagnetic (EM) field, coupled by a static, periodic magnetic lattice, called *undulator*. The electrons themselves generate EM radiation by the process of synchrotron radiation when encountering the magnetic field inside the undulator.

This chapter describes the most important aspects of the theory behind the FEL process, starting from synchrotron radiation and moving to FEL amplification. The final aim is to characterize the most important features of SASE and seeded FELs. It is by no means an exhaustive description, but it highlights useful notions and parameters for the following chapters.

2.1 Synchrotron radiation

The fundamental physical phenomenon that makes all synchrotron lightsources possible (including FELs) is synchrotron radiation. According to classical electrodynamics[23], when a charged particle, accelerated to relativistic velocities, encounters a static magnetic field, it produces a broad band radiation called synchrotron radiation. We begin our description of the FEL process by analyzing the synchrotron radiation from a particle moving on a curved path, determining the power distribution of this radiation as a function of solid angle.

We define a few useful quantities for a relativistic particle moving with velocity $\vec{v}$:

- the scaled velocity $\vec{\beta} = \frac{\vec{v}}{c}$ with $|\vec{\beta}| < 1$

- the scaled acceleration $\dot{\vec{\beta}} = \frac{d\vec{v}}{dt}\frac{1}{c}$
- the scaled total energy, or Lorentz factor $\gamma = \frac{E_{tot}}{E_{rest}} = \frac{1}{\sqrt{1-\beta^2}}$

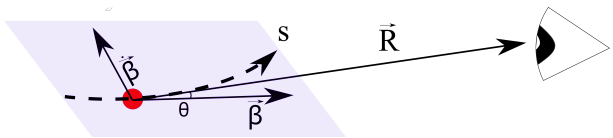

Figure 2.1: Schematic drawing of the motion of a relativistic particle (red dot) as viewed from a laboratory frame of reference

In the simple case of a particle moving along a curved path S, shown in figure 2.1, the scaled velocity $\vec{\beta}$ and acceleration $\dot{\vec{\beta}}$ define the plane of movement. The position of an observer, in the laboratory frame of reference, is defined by the vector $\vec{R}$ w.r.t. the particle. From classical electrodynamics[23], we find that the electric field $\vec{E}$, produced by the considered charged particle, is calculated using the Liénardt-Wiechert retarded potentials as:

$$\vec{E} = \frac{e}{4\pi\epsilon_0}\left[\underbrace{\frac{\vec{n}-\vec{\beta}}{\gamma^2(1-\vec{n}\cdot\vec{\beta})^3|\vec{R}|^2}}_{\text{Coulomb term}} + \underbrace{\frac{\vec{n}\times(\vec{n}-\vec{\beta})\times\dot{\vec{\beta}}}{c(1-\vec{n}\cdot\vec{\beta})^3|\vec{R}|}}_{\text{Radiation term}}\right]_{ret} \tag{2.1}$$

where $\vec{n} = \frac{\vec{R}}{|\vec{R}|}$ and the index $_{ret}$ is used to remind us that the quantities are to be evaluated at the retarded time $t_r = t - \frac{|R|}{c}$. In the "far-field" approximation, where R is large, only the radiation term in equation 2.1 remains, since it only falls as $1/R$ while to Coulomb term falls as $1/R^2$.

The radiated power per unit of solid angle $d\Omega$, in the laboratory frame of reference is given by:

$$\frac{dP}{d\Omega} = \vec{S}\cdot\vec{n}(1-\vec{n}\cdot\vec{\beta})R^2 \tag{2.2}$$

where $\vec{S} = \frac{1}{\mu_0}|\vec{E}|^2\cdot\vec{n}$ is the Poynting vector.

For synchrotron radiation we consider the particles to be ultra-relativistic, $\beta \to 1$ and the observer to be far away from the source, in the "far-field" region. Thus the angular power distribution becomes:

$$\frac{dP}{d\Omega} \approx \frac{8e^2\dot{\vec{\beta}}^2}{\pi c}\gamma^8\frac{\gamma^2\theta^2}{(1+\gamma^2\theta^2)^2}. \tag{2.3}$$

The resulting power distribution is highly dependent on the angle θ between the deflecting plane and the observation direction; the power is emitted in a small cone of angle $\theta = 1/\gamma$.

We note here that equation 2.3 also describes the emission of coherent synchrotron radiation which can have unwanted effects on the electron and is one of the main discussion points in **paper IV**.

Integrating over all angles we find the total emitted power to be:

$$P = \frac{2}{3}\frac{e^2}{4\pi\epsilon_0 c}\gamma^6\left[\dot{\beta}^2 - (\vec{\beta}\times\dot{\vec{\beta}})^2\right]. \tag{2.4}$$

Equation 2.4 indicates that the Power emitted is highly dependent on the motion of the particle, i.e., the angle between $\dot{\vec{\beta}}$ and $\vec{\beta}$. Furthermore the dependence on γ^6 suggests that the electron should be the particle of choice for synchrotron radiation lightsources, as its rest energy is much smaller compared to other charged particles.

In a constant magnetic field $\vec{B}$ perpendicular to their velocity $\vec{v}$, such as that of a bending magnet or undulator, electrons follow a circular trajectory with the radius $\rho = \frac{c\beta m}{Be}$. The acceleration in this case is $\dot{\beta} = \frac{-e}{\gamma m}\beta B$. Thus the total emitted power simplifies to:

$$P = \frac{e^2}{4\pi\epsilon_0 m^2 c}(\gamma\beta B)^2. \tag{2.5}$$

2.2 Undulator radiation

The periodic magnetic array in which the electrons and the radiation interact during the FEL process is called undulator and it is arguably the most important part of a FEL. The most common type of undulator is a planar one, for which the magnetic field as a function of position z is described by: $\vec{B}(z) = B_0\sin(k_u z)\hat{e}_y$, where $k_u = \frac{2\pi}{\lambda_u}$ and λ_u is the period of the undulator.

To calculate the power and wavelength of the radiated field we must first find the motion of the electron inside the undulator. In figure 2.2 we sketch the electron trajectory through the undulator. If we assume an initial velocity along the z direction, the electron will experience a magnetic force of $\vec{F}_{mag} = \gamma m_e c\dot{\vec{v}} = -e\vec{v}\times\vec{B}$ perpendicular to its velocity. This yields two coupled equations of motion:

$$\ddot{x} = \frac{e}{\gamma m_e}B\dot{z}, \tag{2.6a}$$

$$\ddot{z} = -\frac{e}{\gamma m_e}B\dot{x}, \tag{2.6b}$$

where $\dot{x}$ symbolizes a derivative w.r.t. time, which will be solved in two steps. First we assume $\ddot{z} = 0$ and find the solution for x to be:

$$x(t) = \frac{K_u}{\gamma\beta k_u} \sin(k_u \beta c t), \tag{2.7a}$$

$$v_x = \dot{x} = \frac{K_u c}{\gamma} \cos(k_u \beta c t), \tag{2.7b}$$

with the undulator parameter $K_u = \frac{eB}{m_e c k_u}$.

Next we acknowledge that the electron is highly relativistic and that the two velocity components satisfy the equation $\dot{z} = v_z = \sqrt{v^2 - v_x^2}$ and find:

$$v_z(t) = \sqrt{c^2 - v_x^2(t)} = \underbrace{\left[1 - \frac{1}{2\gamma^2}\left(1 + \frac{K_u^2}{2}\right)\right]}_{\text{average velocity } \langle v_z(t)\rangle / c = \bar{\beta}} c - \frac{c K_u^2}{4\gamma^2} \cos(2\bar{\beta} c t). \tag{2.8}$$

In equation 2.8 we obtained a new, "average" scaled velocity $\bar{\beta}$ that takes into account the curved motion in the undulator. We can thus refine equation 2.7b to account for the average velocity:

$$\dot{x} = v_x = \frac{K_u c}{\gamma} \cos(k_u \bar{\beta} c t). \tag{2.9}$$

When referring to the velocity along z inside the undulator we always refer to $\bar{\beta}$.

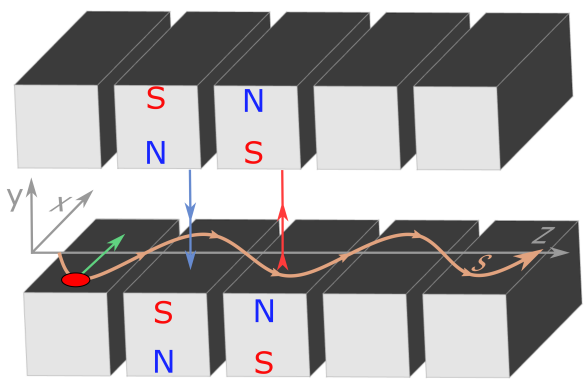

Figure 2.2: The electron's (red dot) motion in an undulator along the path *S* and the magnetic force acting on the electron (green arrow).

2.2.1 Undulator radiation wavelength

The periodic motion of an electron in an undulator gives rise to radiation with a periodic time structure. To calculate the frequency, or wavelength, of the emitted radiation we first consider a coordinate system moving along the z direction with $\bar{\beta}c$. For this system we have the following Lorentz transformations:

$$t^* = \bar{\gamma}(t - \bar{\beta}z/c) \approx \frac{t}{\bar{\gamma}}, \tag{2.10a}$$

$$x^* = \frac{K_u}{\gamma k_u}\sin(\bar{\beta}ct), \tag{2.10b}$$

$$z^* = \bar{\gamma}(z - \bar{\beta}ct), \tag{2.10c}$$

$$\text{with } \bar{\gamma} = \frac{1}{\sqrt{1-\bar{\beta}^2}}, \tag{2.10d}$$

where the * symbol is used to denote quantities in the moving frame of reference.

As we are describing a periodic motion, we can write $x^*(t^*) = A\sin(\omega^* t^*)$. Taking into account the Lorentz transformations, the electron "sees" a magnetic field oscillating with frequency:

$$\omega^* = \bar{\gamma}\bar{\beta}ck_u \approx \frac{\gamma ck_u}{\sqrt{1 + K_u^2/2}}. \tag{2.11}$$

Therefore, in this moving frame of reference the radiated field has the frequency ω^*. An observer in the laboratory frame, far away on the z axis, will measure a frequency of the radiated field $\omega_l = \frac{\omega^*}{\bar{\gamma}(1-\bar{\beta})}$ due to a Doppler shift of $\frac{1}{\bar{\gamma}(1-\bar{\beta})}$. The wavelength of such radiation, on axis, is given by the famous undulator resonance condition:

$$\lambda_l = \frac{2\pi c}{\omega_l} = \frac{\lambda_u}{2\gamma^2}\left(1 + \frac{K_u^2}{2}\right). \tag{2.12}$$

2.3 Electron interaction with radiation inside the undulator

Free-electron lasers rely on the interaction between the electromagnetic radiation, the electrons and the periodic magnetic field of the undulators. To describe this interaction we assume a plane monochromatic light wave:

$$E(z,t) = \frac{E_0}{\sqrt{2}}\exp(i(k_r z - \omega_r t + \phi_0))\hat{e}_x \text{ with } k_r = \frac{\omega_r}{c} = \frac{2\pi}{\lambda_r} \tag{2.13}$$

co-propagating with the electrons inside the undulator. The rate of energy exchange between the electrons traveling through the undulator and the EM field is given by:

$$mc^2 \frac{d\gamma}{dt} = -e\vec{v} \cdot \vec{E}. \tag{2.14}$$

Since the EM field propagates along the z direction, equation 2.14 tells us that the interaction is mediated by the transverse component of the electron velocity v_x. Using equation 2.9 we find that the expression for energy transfer becomes:

$$mc^2 \frac{d\gamma}{dt} = -\frac{ecK_u E_0}{2\gamma} \cos(k_r z - \omega_r t + k_u z + \phi_0) \tag{2.15}$$

where $k_r z - \omega_r t + k_u z + \phi_0 = \psi$ is called the ponderomotive phase and it holds the key to efficient energy transfer from the electron beam to the radiation field. Figure 2.3 illustrates how the ponderomotive phase determines whether an electron gains or loses energy to the EM field. Using the fact that we know the average velocity $\bar{\beta}c$ along z, we make the conversion between the z and t variables as $z(t) = \bar{\beta}ct$ and find the time dependent expression for the ponderomotive phase:

$$\psi(t) = [(k_r + k_u)\bar{\beta}c - \omega_r]t + \phi_0. \tag{2.16}$$

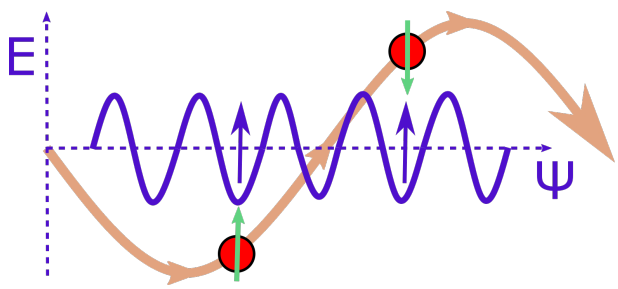

Figure 2.3: Interaction between EM wave (purple) and electrons (red dots). The electrons following the same trajectory (brown line) can either take (green arrow up) or give (green arrow down) energy to the field.

The amount of energy transfer depends solely on the value of ψ, therefore to maximize energy transfer we need to impose the condition $\psi(t) = 2n\pi$. There is a single wavelength of the EM field that can fulfil the condition of $\psi(t) = ct$:

$$\begin{aligned} \frac{d\psi}{dt} = 0 \Leftrightarrow k_r(1-\bar{\beta}) = k_u\bar{\beta} \Leftrightarrow \lambda_r = \lambda_u \frac{\bar{\beta}}{1-\bar{\beta}}, \\ \lambda_r = \frac{\lambda_u}{2\gamma^2}\left(1 + \frac{K_u^2}{2}\right). \end{aligned} \tag{2.17}$$

One might notice that the condition for maximal energy transfer (equation 2.17) is the same as the wavelength of the spontaneous radiation from undulator (equation 2.12). This result is extremely important as it allows the electrons to transfer energy to the field generated by their own spontaneous radiation in the undulators, which is the basic mechanism of FEL amplification.

2.3.1 The separatrix

Figure 2.3 suggests that for electrons with not too high energies, the field acts as a potential well, bounding the motion of the electrons in ψ. To show this, we allow electrons to have non-ideal energies and we parameterize this energy deviation by:

$$\eta = \frac{\gamma - \gamma_r}{\gamma_r}, \text{ with } \gamma_r = \sqrt{\frac{\lambda_u}{\lambda_r}\left(1 + \frac{K}{2}\right)}.$$

We can write the Hamiltonian of the system composed of an electron and EM radiation in terms of the variables ψ and η:

$$H(\psi, \eta) = k_u c\eta + \frac{eE_0K}{2mc\gamma_r^2}(1 - \cos(\psi)). \tag{2.18}$$

The above equation describes, for stable values of ψ and η a pendulum motion, which we call "synchrotron oscillations" with frequency:

$$\Omega_{sync} = \sqrt{\frac{eE_0Kk_u}{m_e\gamma_r^2}}. \tag{2.19}$$

The curves in figure 2.4 depict motions in the (ψ, η) phase space. For values of the Hamiltonian $H \leq c\Omega^2/k_u$ the motion is bounded, while if $H = H_{sep} = c\Omega^2/k_u$ the motion takes the blue path, called the separatrix. The separatrix curve is parameterized in[6] as:

$$\eta_{sep}(\psi) = \pm\sqrt{\frac{eE_0K}{2k_umc\gamma_r^2}}\cos(\psi/2). \tag{2.20}$$

In the (ψ, η) phase space, the separatrix therefore defines a region in which the electrons are able to oscillate around the reference point (0,0), but cannot escape. Through the motion in this phase space "bucket", always clock-wise, electrons can "bunch" together around the same phase, creating a longitudinal high density region. This

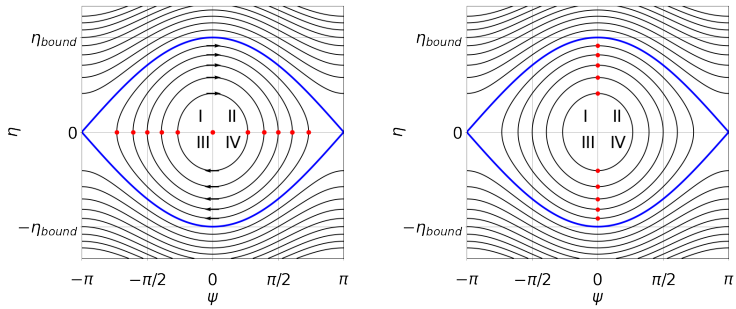

Figure 2.4: Electron (red dots) trajectories (black curves) in the (η, ψ) phase space bounded by the separatrix (blue curve). Snapshot in the motion of the electrons when all have 0 energy deviation (left) and when all have 0 phase deviation (right).

process is the fundamental mechanism for creating the periodic micro-bunches in the FEL process.

2.4 Fundamentals of high gain FEL theory

The motion described by equation 2.18 is valid under the assumption that the field amplitude is constant through the propagation along the undulator, i.e., the gain of the radiation $G = \frac{P_{out}-P_{in}}{P_{in}} \approx 0$. However, we want to transfer GW of power from the electrons to the radiation and therefore dispense with the constant field amplitude assumption. The field is allowed to vary in amplitude along z by slightly modifying equation 2.13 into:

$$\tilde{E}(z,t) = \frac{\tilde{E}_0(z)}{\sqrt{2}} \exp(i(k_r z - \omega_r t + \phi_0))\hat{e}_x \tag{2.21}$$

where $\tilde{E}$ denotes the complex field. The actual field is obtained by taking the real part $E = \Re(\tilde{E})$.

Furthermore, we exchange the picture of single electrons traveling alone in the undulator with that of an electron bunch, characterized by a complex charge $\tilde{\rho}(\xi, z)$ and current $\tilde{j_z}(\xi, z)$ densities.

2.4.1 The 1D model

In the following, we restrict our description to the 1D model, in which the beam is assumed to have no spread in the (x,y) plane nor any spread in the velocity components

v_x and v_y. Although this assumption ignores transverse effects such as photon and electron beam alignment, it is sufficient to quantitatively describe the evolution of the EM field along the undulator.

In a high gain FEL, both the electron density and the field amplitude evolve as they progress along the undulator line. This is mainly due to a self-amplifying process between the beam current density and the radiation field amplitude. The existing EM radiation, along with the undulators' magnetic field, "trap" the electrons inside the separatrix, essentially creating a density modulation in the electron beam. Due to the energy exchange condition (equation 2.17), the density modulation period exactly matches the EM radiation wavelength. As the modulation density increases so does the number of electrons radiating in phase. The more electrons radiate in phase, the higher the EM field amplitude which in turn creates a larger modulation.

We write the evolution of the charge and current density with an evolving term that has the periodicity of the EM radiation wavelength:

$$\begin{aligned} \tilde{\rho}(\xi, z) &= \rho_0 + \tilde{\rho_1}(z) \exp(i\psi), \\ \tilde{j_z}(\xi, z) &= j_0 + \tilde{j}_1(z) \exp(i\psi). \end{aligned} \tag{2.22}$$

Applying Maxwell's equations [23] to the field, charge and current densities and assuming that the field $\tilde{E}_x$ varies slowly in one undulator period[a] we obtain the following equations:

$$\frac{d\psi_n}{dz} = 2k_u\eta_n, \tag{2.23a}$$

$$\frac{d\eta_n}{dz} = -\frac{e}{mc^2\gamma_r}\Re\left\{\left(\frac{\hat{K_u}\tilde{E}_x}{2\gamma_r} - \frac{i\mu_0 c^2}{\omega_r}\right)\exp(i\psi_n)\right\}, \tag{2.23b}$$

$$\tilde{j} = j_0\frac{2}{N_e}\sum_{n=1}^{N_e}\exp(-i\psi_n), \tag{2.23c}$$

$$\frac{d\tilde{E}_x}{dz} = -\frac{\mu_0 c\hat{K}_u}{4\gamma_r}\tilde{j}_1, \tag{2.23d}$$

where E_x is the component along the x direction of the EM field, n represents the index over all N_e electrons in the bunch, $\tilde{K}_u = K_u\left[J_0\left(\frac{K_u^2}{4+2K_u^2}\right) - J_1\left(\frac{K_u^2}{4+2K_u^2}\right)\right]$ is the modified undulator parameter to account for the electron oscillations in z and J_ν is the Bessel function of the ν^{th} order.

[a] This approximation is called the slow varying envelope (SVEA) and it is used by most FEL simulation codes

The $2N_e+2$ sub-equations in equation 2.23 form the coupled, first order equations for 1D high gain FEL. Unfortunately, they cannot be solved analytically, but numerical integration codes such as AURORA[24] or a 3D simulation code, like Genesis 1.3[25] offer a reliable way of obtaining both the current density and field intensity for a high gain FEL.

An analytical solution can be found for the field by assuming that the periodic density modulations are small, thus eliminating the equations in ψ_n and η_n. The coupled sub-equations in equation 2.23 become a single differential equation for the field:

$$\frac{d^3E_x}{dz} + 4ik_u\eta\frac{d^2E_x}{dz^2} + (k_p^2 - 4k_u^2\eta^2)\frac{dE_x}{dz} - i\Gamma_{FEL}E_x = 0, \tag{2.24a}$$

$$\text{with } \Gamma_{FEL} = \left[\frac{\mu_0\hat{K}e^2k_un_e}{4\gamma_r^3m_e}\right] and k_p = \sqrt{\frac{2k_u\mu_0n_ee^2c}{\gamma m_e\omega_r}}.$$

One can solve equation 2.24a by assuming an incident wave E_{in}. This leads to three solutions: an exponentially damped one, an oscillating part and the one in which we are interested, the exponentially growing part:

$$|\tilde{E_x}(z)| = \frac{E_{in}}{3}\exp\left(\frac{z\sqrt{3}}{2\Gamma_{FEL}}\right), \tag{2.25a}$$

or in terms of Power

$$P = \frac{P_{in}}{9}\exp\left(\frac{z\sqrt{3}}{\Gamma_{FEL}}\right). \tag{2.25b}$$

Equation 2.25a describes the FEL process as the exponential amplification of an initial EM field, by the transfer of energy from the electron beam to the field. The exponential growth suggests the definition of gain length $L_g = \frac{\sqrt{3}}{\Gamma_{FEL}}$ over which the power increases by a factor e. Γ_{FEL}, or rather, $\rho_{FEL} = \frac{\Gamma_{FEL}}{2k_u}$ is called the Pierce parameter or FEL parameter and it holds a special place in the analytical estimations of FELs, being present in almost all important parameters describing a FEL, from bandwidth to energy extraction efficiency.

The amplification is not unbounded, with saturation being reached after a certain energy is transferred from the electrons to the EM radiation. The efficiency of energy transfer is in the order of the Pierce parameter ρ_{FEL}. Given the total power of the electron beam $P_{beam} = \frac{\gamma_r mc^2 I}{e}$, where I is the beam current, the power of the EM field at saturation is :

$$P_{sat} \approx \rho_{FEL}P_{beam}. \tag{2.26}$$

As it is impossible to create a beam where all electrons have exactly the same energy, we can define an initial spread in energy $\sigma_\eta = \sqrt{\langle {\eta_n}^2 \rangle_n}$, where $\langle ... \rangle_n$ signifies the average over the index n. Under non-zero energy spread conditions the gain length increases since not all electrons can be trapped in the FEL "bucket", reducing the energy transfer efficiency. It was shown[6] that for an energy spread of $\sigma_\eta = 0.5\rho_{FEL}$ the gain length increases by 25 %.

2.4.2 3D effects

For certain conditions of the electron beam and radiation wavelength it can be crucial to take into account 3D effects. The analytical treatment of the 3D FEL process is significantly more complicated therefore, in this section, we limit ourselves to highlighting the most important effects with a full derivation available in (Schmuser 2009)[6].

In the transverse plane, the motion of one electron is defined by 2 position coordinates (x, y) and 2 velocity coordinate (v_x, v_y). The full motion is described by the 6D vector:

$$(x, y, z, v_x, v_y, \gamma) \text{ or } (x, y, \psi, x', y', \gamma). \tag{2.27}$$

Simulation codes usually use a frame of reference moving with the beam (along the path S in figure 2.2) and thus use ψ instead of z, $x' = v_x/v$ instead of v_x and $y' = v_y/v$ instead of v_y as particle coordinates.

In describing an electron beam it is useful to define a reference particle, with ideal coordinates $(x_0, y_0, \psi_0, x'_0, y'_0, \gamma_0)$, so all other particles are then defined w.r.t. this idealized one. The beam itself is described by statistical quantities that take into account all the electron's positions and angles. Here we present the most important ones:

$$\text{size: } \sigma_x = \sqrt{\langle x^2 \rangle_n}\ ,\ \sigma_y = \sqrt{\langle y^2 \rangle_n}, \tag{2.28a}$$

$$\text{divergence: } \sigma_{x'} = \sqrt{\langle x'^2 \rangle_n}\ ,\ \sigma_{y'} = \sqrt{\langle y'^2 \rangle_n}, \tag{2.28b}$$

$$\text{emittance: } \epsilon_x = \sqrt{\sigma_x \sigma_{x'} - \langle x x' \rangle_n}\ ,\ \epsilon_y = \sqrt{\sigma_y \sigma_{y'} - \langle y y' \rangle_n}. \tag{2.28c}$$

In measurements, however, a more useful form for emittance is the energy normalized emittance $\epsilon_n = \epsilon \cdot \gamma$, which is preserved during acceleration.

To keep high electron densities, the beam's transverse size must be kept low. This is done through "strong focusing"[26] by inserting quadrupole magnets between undulator sections, ensuring the transverse size of the beam does not grow enough to ruin the FEL process.

As all EM radiation, FEL radiation diffracts, increasing its transverse size with increasing z position. However, since in the high gain regime the field intensity increases exponentially, more radiation will be produced in a gain length than in all the undulator line before it. This means that even though radiation generated earlier in the FEL process will diffract, the newly produced radiation will have roughly the same size as the electron beam. Close to the position z_{sat}, where power saturation occurs, the radiation will have its lowest transverse size since around this point the most radiation within a gain length is produced. This effect is know in FEL literature as *gain guiding*.

Taking into account the beam's transverse size, radiation diffraction and electron energy spread, Ming Xie[27] developed a way to calculate $F(\epsilon_{x,y}, \sigma_{x,y}, \sigma_\eta)$, a correction term to the 1D gain length and saturation power estimations. This correction always increase the gain length $L_{g3D} > L_{g1D}$ and reduce the power $P_{sat\_3D} < P_{sat\_1D}$ estimations.

Based on the initial conditions at the beginning of the FEL, such as initial field or current density, one can distinguish two types of FEL: SASE (Self Amplified Spontaneous Emission) and Seeded. The SASE process relies on initial statistical fluctuations in the electron beam density to start the FEL process, while seeded FEL either have a seed laser or some pre-modulation of the electron beam to overcome the randomness of spontaneous emission.

2.5 The SASE FEL

As the name suggests, self amplified spontaneous emission (SASE) FELs amplify spontaneous radiation generated by the beam itself in the first few meters of the undulator. Because we can never create a perfectly smooth, high current, electron beams, the initial current density will have a random distribution of modulation frequencies. Following the derivations in (Schmuser)[6], the electron beam's randomness results in a frequency distribution in the EM field. The rms spread of this distribution as a function of position along the undulator has the form:

$$\sigma_\omega(z) = 3\sqrt{2}\rho_{_{FEL}}\omega_l\sqrt{\frac{L_g}{z}}. \tag{2.29}$$

In SASE the saturation occurs roughly after 20 gain lengths[6], therefore at saturation the spectrum will be narrowest $\sigma_{\omega\_sat} \approx \rho_{_{FEL}}\omega_l$.

To better understand the spectral distribution of SASE radiation we can use figure 2.5 in which we have a typical SASE spectrum plotted on the left and an average of multiple shots plotted on the right. We can see that a SASE spectrum consists of numerous

narrow peaks with random intensities. The width of one of these spikes $\delta\omega$ is related to the length Δt_{bunch} of the radiating electron bunch as $\delta\omega = 1/\Delta t_{bunch}$. The total number of spikes is given by the number of longitudinal modes $M_f = L_{bunch}/l_c$ where $l_c = \lambda_r/(4\pi\rho_{FEL})$ is the coherence length and L_{bunch} is the bunch length. The shot to shot variations are large but the overall shape tends towards a smooth distribution, suggesting that the process behind SASE is a random one.

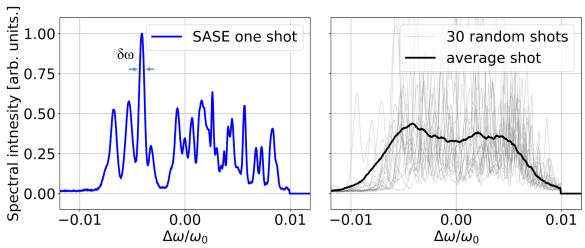

Figure 2.5: (left) Typical SASE spectrum. (right) Multiple SASE spectra of the same FEL (gray) and average SASE spectra (black).

The relatively large bandwidth of SASE, $\Delta\lambda/lambda \approx 10^{-3}$ can be explained by the "noisiness" of the current distribution. The FEL process preferentially amplifies radiation produced in high current regions of the electron bunch. Since these regions are randomly distributed within the bunch, the radiation produced in a particular region will have a random phase relation to radiation coming from another region. The limited coherence length l_c[b] translates into a relatively broad spectrum with random spikes, as seen in figure 2.5.

2.6 Coherence improvements by seeding

A way to improve on the longitudinal coherence of SASE is to create "order" in the electron beam through seeding. Depending on the the mechanism of choice, there are numerous hardware configurations that can be used to seed a FEL. In figure 2.6 we sketch the layout of a few of the most common FEL modes of operation. Th simplest mode is SAE, which does no have any seeding, continuing in order of conceptual complexity, one might find direct seeding, then "self-seeding", followed by seeding at a harmonic of a laser in schemes like HGHG and EEHG.

A way to generate long distance order within the electron beam is needed in order to improve the coherence length. A natural solution is to simply have a conventional laser, which has constant phase relation throughout the pulse, "seed" the electron

[b]We address the meaning of coherence length in chapter 3.1

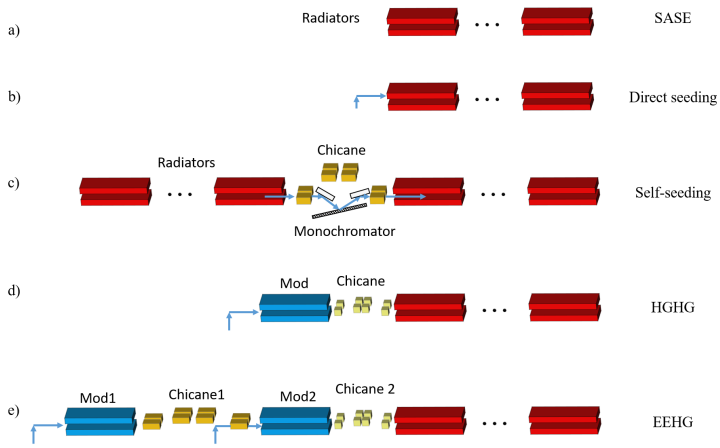

Figure 2.6: Different types of seeding options a: SASE b: Direct seeding c: Self-seeding d: High gain harmonic generation (HGHG) e: Echo enable harmonic generation (EEHG)

distribution (figure 2.6-b). If the laser has sufficient power to overcome the shot-noise, it will imprint an energy and then a density modulation over the entire electron beam. This will create the desired long-distance order and almost all the electrons will eventually radiate with the same phase.

This type of seeding is called *direct seeding* and it was proven [28] to significantly improve the spectral quality of FELs.

However, conventional lasers do not have sufficient power for the short wavelengths that SASE FELs are capable of reaching (from soft to hard X-rays), so another way of creating the long-range correlation is needed.

Self-seeding (figure 2.6-c) FELs can reach all the wavelengths a regular SASE FEL can reach. The method involves producing SASE radiation, passing it through a monochromator and then allowing the resulting EM radiation to "seed" the electron beam in a new undulator line. The monochromator selects only one spectral component, out of the many existing in the SASE spectrum, thus obtaining the long distance order. This technique is however subject to very large intensity fluctuations. Because the wavelength selected by the monochromator is fixed for all shots and SASE has shot to shot variation in intensity at a fixed wavelength, the monochromatized radiation can vary in intensity as much as 100 %.

In the following we present a two ways of seeding in the UV to soft X-ray limit at a harmonic of a seed laser. To understand these seeding schemes it is worthwhile to explain the concept of **bunching**. As the electron beam distribution starts to develop density modulations, we can find the percentage of the beam that is modulated at a

specific wavelength λ_b using the bunching statistical function. If we assume that the electron beam is characterized by a distribution in z and γ $f(z,\gamma)$, the bunching for this distribution as a function of bunching wavelength λ_b is:

$$b(\lambda_b) = \left| \frac{\int_{-\infty}^{\infty} f(z) \exp(-i\frac{z2\pi}{\lambda_b})\, d\xi}{\int_{-\infty}^{\infty} f(z)\, dz} \right|, \quad \text{with } f(z) = \int_{-\infty}^{\infty} f(z,\gamma) d\gamma. \tag{2.30}$$

2.6.1 Chicanes and CSR

Most seeding techniques use a 4 bending magnet array called a *Chicane* to affect the longitudinal phase space (z,γ). The principle of the Chicane is explained in figure 2.7. We use three electrons that are color-coded to represent how energetic they are, (blue-low green-medium and red-high) to define a bunch. As they are all highly relativistic, they essentially have the same velocity c, the difference in energy translates therefore, in a difference in mass. More energetic electrons will be bent les by the magnetic field in the bending magnets with the opposite being valid for less energetic electrons. Therefore electrons with different energies will take different paths through the Chicane which will result in them moving relative to each other in the z direction. The strength of a Chicane is calculated based on how much an electron with energy deviation $\Delta\gamma$ moves in z w.r.t. the reference electron:

$$R_{56} = \frac{\Delta\gamma}{\gamma_0}\Delta z. \tag{2.31}$$

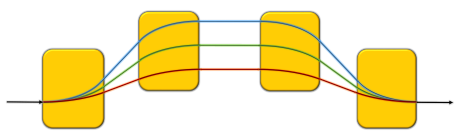

Figure 2.7: Working principle of a 4 bending magnet (yellow squares) Chicane, in which low energy electrons (blue) take a longer path that nominal (green) or high (red) energy electrons.

The synchrotron radiation in bending magnets, such the ones in a Chicane, has a broadband frequency range[29]. As we have seen in in **chapter 2.4.1**, if electrons radiate in phase the intensity of the emitted radiation increases greatly. This means that under the strong magnetic field of a bending magnet the electron bunch will emit radiation, coherently, at the wavelengths close to the bunch length.

Furthermore, because the electrons have a transverse component to their velocity due to the bending magnet, they will interact with the the radiation produced by the bunch itself. Among other effects like increasing energy spread and emittance[30,31], the CSR will modulate the energy of the electron bunch at this long wavelength.

Because of the dependence on the retarded time t_r of synchrotron radiation, the head of the beam will experience the field generated by the tail of the beam. The energy change ΔE[32] as a function of position s in the bunch with a Gaussian current profile $\sigma_s = 25\mu m$ of peak current $I_0 = 1kA$ is shown in figure 2.8.

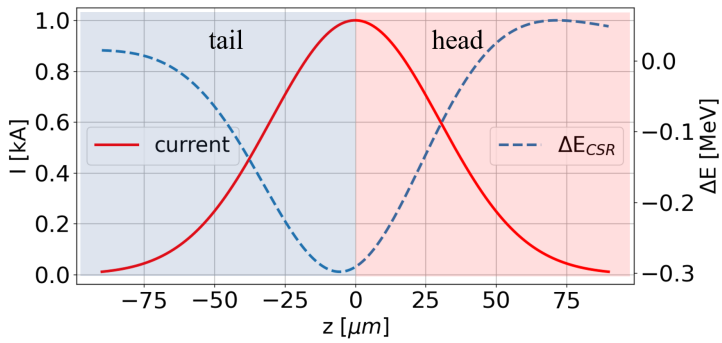

Figure 2.8: Current profile along the bunch (red line) and CSR induced energy change (dashed blue line) for a beam after passing through a bending magnet. The "head" and "tail" regions of the beam are marked by a red and blue background respectively.

Even though we only presented here the case of CSR generated in a Chicane, the approach is similar for any dispersive section (DS) that uses bending magnets.

2.6.2 High Gain Harmonic Generation

Once significant bunching at a specific wavelength λ_0 exists, there is also some bunching at the a^{th} harmonic of this wavelength λ_0/a. This suggests that if one can create sufficient bunching at the "seed" laser wavelength then it is possible to lase, in a second stage called lasing, at a harmonic of the initial seed.

In high gain harmonic generation (HGHG, figure 2.6-d) an energy modulation is imprinted on the beam by the seed laser in an undulator tuned to the wavelength λ_0 of the seed. The energy modulation is transformed into density modulation with a Chicane and so bunching is created at the laser wavelength. Because bunching also exists at higher harmonics of the fundamental, it is possible to set the radiators (a series of undulators in which the FEL process occurs) to the resonant wavelength

$\lambda_{rad} = \lambda_0/a$ and still have a "seeded" FEL. This process is, however, limited in the order of the achievable harmonic to $a \approx 10$.

An extension to this idea is the two step harmonic conversion. In this scheme the harmonic radiation produced in the first step is used as the "seed" for the second step allowing for a radiation at harmonic $a_{final} = a_{step1} \cdot a_{step2}$. There are, however, some disadvantages to this method such as increasing the energy spread of the electron beam in the first step/stage. For this reason a the FERMI FEL- 2[33] a "fresh-bunch" technique was implemented. In this option only a portion of the bunch is used in the first stage so that the second stage might be implemented in the un-spoiled, "fresh", part of the bunch.

2.6.3 Echo Enabled Harmonic Generation

Echo Enabled Harmonic Generation (EEHG)[14] is a seeding technique that uses two modulator-Chicane [d] combinations to create significant bunching at high harmonics of a seed laser (see figure 2.6-e). In the first modulator the electron beam gets an energy modulation at the wavelength λ_{mod_1}, this energy modulation is then transformed into very thin energy stripes using a dispersive section (DS1). A second modulator (Mod 2) imprints a second energy modulation at λ_{mod_2} wavelength with the second dispersive section (DS2) transforming the energy stripes into high frequency density modulations (figure 2.9-e).

Throughout this thesis, whenever referring to EEHG, we closely follow the scaled notations for longitudinal phase space used by (Xiang and Stupakov)[34]:

$$p = \frac{\gamma - \gamma_0}{\sigma_\gamma} \tag{2.32a}$$

$$\xi = \frac{z 2\pi}{\lambda_{mod\_1}} \tag{2.32b}$$

with σ_γ the rms energy spread. The energy modulation amplitudes and Chicane strengths are also transformed into scaled quantities:

$$A_i = \frac{\Delta\gamma_i}{\sigma_\gamma} \tag{2.33a}$$

$$B_i = R_{56\_i} \frac{2\pi}{\lambda_{mod\_1}} \frac{\sigma_\gamma}{\gamma_0} \tag{2.33b}$$

with $\Delta\gamma_i$ being the energy modulation in modulator i, R_{56_i} the strength of DSi and γ_0 the reference energy.

[d] In the original proposal the authors used two chicanes, but any "dispersive section" which moves the electrons along z based on their energy can be used.

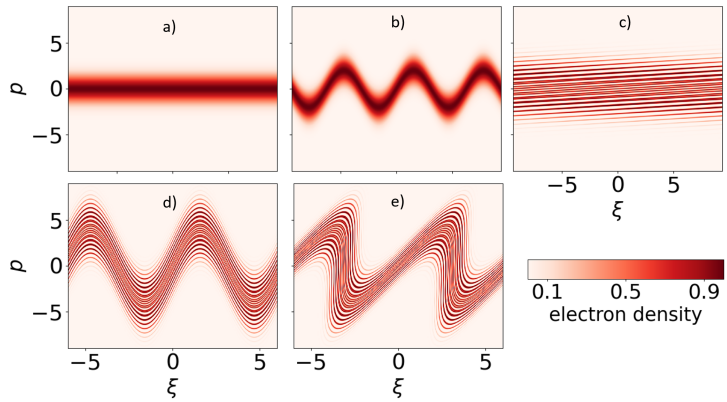

Figure 2.9: Phase space transformations through the EEHG harmonic conversion scheme. a: initial beam. b: beam after modulator 1. c: beam after DS1 d: beam after modulator 2. e: beam after DS2.

Because the final phase space has a complicated shape, we complement the mathematical description with a step-wise illustration of the longitudinal phase space in figure 2.9.

We start by considering a normally distributed electron beam in energy, p, with a flat top current, i.e., no dependence on ξ. In the first modulator the beam is modulated with amplitude A_1 transforming the p coordinate as $p_1 = p + A_1 \sin(\xi)$ (figure 2.9-b). The first DS shifts the electrons in ξ based on their energy p_1 as $\xi_1 = \xi + B_1 p_1$ (figure 2.9-c). The second modulator transforms p as $p_2 = p_1 + A_2 \sin(\xi_1 + \phi)$ (figure 2.9-d) while the final DS transforms ξ to be $\xi_2 = \xi_1 + B_2 P_2$ (figure 2.9-e). All the transformations a particle with initial coordinate (ξ, p) undergoes in the EEHG scheme can be summarized by:

$$p_1 = p + A_1 \sin(\xi) \tag{2.34a}$$
$$\xi_1 = \xi + B_1 p_1 \tag{2.34b}$$
$$p_2 = p_1 + A_2 \sin(K\xi_1 + \phi) \tag{2.34c}$$
$$\xi_2 = \xi_1 + B_2 P_2 \tag{2.34d}$$

where $K = \frac{\lambda_{mod\_1}}{\lambda_{mod\_2}}$.

We assume $f_0(\xi, p) = \frac{N_e}{\sqrt{2\pi}} e^{-p^2/2}$ to be our initial phase space distribution, with N_e the number of electrons. It can be shown[34] that the final distribution takes the form:

$$f_{EEHG}(\xi, p) = \frac{N_0}{\sqrt{2}} \exp\Big[\frac{-1}{2}(p - A_2 \sin(K\xi - KB_2 p + \phi) - A_1 \sin(\xi - (B_1 + B2)p + A_2 B_2 \sin(K\xi - KB_2 p + \phi)))^2\Big]. \tag{2.35}$$

If we apply the bunching formula in equation 2.30 to the final distribution of the EEHG seeding scheme, taking into account the coordinate transformations (equation 2.32) we find:

$$b = \frac{1}{N_0}\int_{-\infty}^{\infty} f_0(p)e^{-iap(B_1+B_2)}dp\times$$
$$\langle e^{-ia\xi}e^{-iaA_1(B_1+B_2)\sin\xi}e^{-iaA_2B_2\sin(K\xi+KB_1+KA_1B_1\sin\xi+\phi)}\rangle. \tag{2.36}$$

Equation 2.36 can be simplified if, for every exponential term with ξ, one uses the series expansion of the form[35]:

$$e^{i\alpha\sin(x)} = \sum_{\nu=-\infty}^{\infty} e^{i\nu x}J_\nu(\alpha) \tag{2.37}$$

where J_ν is the order ν Bessel function of the first kind.

Carrying out the integration over p, we find the final form of the bunching function for EEHG harmonic seeding:

$$b_{n,m} = \Big|\exp\Big[-\frac{1}{2}(nB_1+(Km+n)B_2)^2\Big]\times\langle e^{i(n+mK-a)\xi}\rangle$$
$$J_m(-(Km+n)A_2B_2)J_n(-A_1(nB_1+(Km+n)B2))\Big|. \tag{2.38}$$

The oscillating function $e^{i(n+mK-a)\xi}$ averages to zero for every (n,m) combination except for the case $a = n+mK$.

In **chapter 6** we will expand on the EEHG scheme to show how A_i and B_i can be chosen to maximize the bunching of the distribution in equation 2.35.

Chapter 3

Coherence

In this chapter, we offer an interpretation of what statistical coherence means and what it can tell us about the FEL radiation. We consider a quite general EM field which has, nevertheless, some key properties that the FEL radiation also has, such as "quasi-monochromaticity" and low divergence. We focus on statistical quantities that are relevant for the measurements presented in **paper III** and for the analysis in **paper IV**.

The aim of the statistical description description of coherence is to provide measurement accessible quantities that characterize the radiation in terms of transverse and longitudinal coherence.

3.1 Statistical description of coherence

We begin assuming an arbitrary electromagnetic wave whose complex electrical field is taken to be $\tilde{E}(\vec{r},t)$. The dependence of the longitudinal profile is encoded in the variable t while its variations in the plane (x,y), transverse to the direction of propagation, is given by the vector $\vec{r}$.

To describe the EM field we use statistical averaging either over many instances of the field, or over a time window T inside the same instance of the field, much larger than the fluctuation time. An example of such a statistical quantity is the averaged intensity:

$$I(\vec{r},t) = \langle |\tilde{E}(\vec{r},t)|^2 \rangle \tag{3.1}$$

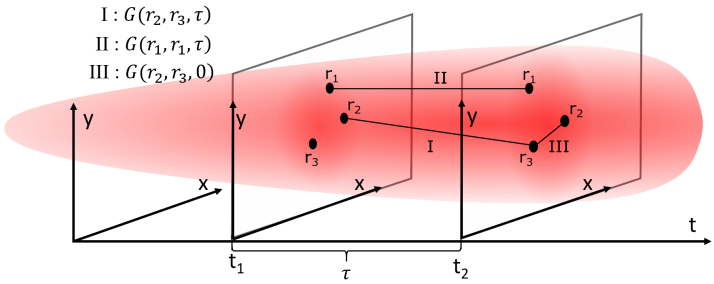

Figure 3.1: Representation of the three types of coherence (I:Mutual coherence, II:Longitudinal coherence and III: Transverse coherence).

where $\langle ... \rangle$ denotes the averaging over the time window T.

In figure 3.1 we represent the EM field with red and we identify three types of possible correlations between different points in the (x,y,t) space.

The field $\tilde{E}(\vec{r}, t)$ is considered to have fluctuations in both time and position. To quantify how correlated the field fluctuations are, we define an averaging function called the *mutual coherence function*[36] (MCF). This statistical function relates the field at position $\vec{r}_1$ and $\vec{r}_2$ given a certain time delay τ (correlation I in figure 3.1):

$$G_{12\tau} = G(\vec{r}_1, \vec{r}_2, \tau) = \left\langle \tilde{E}^*(\vec{r}_1, t)\tilde{E}(\vec{r}_2, t+\tau) \right\rangle \tag{3.2}$$

with its normalized version the **complex degree of coherence** $g_{12\tau}$:

$$g_{12\tau} = g(\vec{r}_1, \vec{r}_2, \tau) = \frac{G(\vec{r}_1, \vec{r}_2, \tau)}{\sqrt{G(\vec{r}_1, \vec{r}_1, 0)G(\vec{r}_2, \vec{r}_2, 0)}} \tag{3.3}$$

with $\tilde{Z}^*$ the complex conjugate of the complex quantity $\tilde{Z}$.

The reader will find that, in equation 3.3, the term $G(\vec{r}_i, \vec{r}_i, 0)$ in the denominator is in fact the averaged intensity at position $\vec{r}_i$. This means that $g_{12\tau}$ is just the $G_{12\tau}$, normalized by the intensities at $\vec{r}_1$ and $\vec{r}_2$, and is thus always bounded between 0 and 1[36].

The function $g_{12\tau}$, is the first expression of coherence for a field. It is used to characterize a field of varying intensity and phase at points $\vec{r}_1$ and $\vec{r}_2$ that have a time delay τ, with high values of $g_{12\tau}$ meaning high levels coherence.

3.1.1 Longitudinal coherence

The fluctuations in time of the EM field at a point $\vec{r}$ in the transverse plane describe how correlated the field is in time. By using the limiting case of $\vec{r}_1 = \vec{r}_2 = \vec{r}$ from equation 3.3, we define a new statistical function, the *autocorrelation* $G_{11\tau}$ function and its normalized version the **complex degree of longitudinal coherence** $g_{11\tau}$:

$$G_{11\tau} = G(\vec{r}, \tau) = \langle \tilde{E}(\vec{r}, t+\tau)\tilde{E}^*(\vec{r}, t) \rangle \tag{3.4}$$

$$g_{11\tau} = g(\vec{r}, \tau) = \frac{G(\vec{r}, \tau)}{G(\vec{r}, 0)}. \tag{3.5}$$

The interpretation of $g_{11\tau}$ is made easier by considering the phase dependence of the quantity $\tilde{u}(\vec{r}, t) = \tilde{E}(\vec{r}, t+\tau)\tilde{E}^*(\vec{r}, t)$. If the fluctuations in phase of the field separated by delay τ are uniform, then the phase of the function $\tilde{u}$ will not vary too much. Therefore, when averaging, it will have a value close to unity. If on the other hand $\tilde{E}(\vec{r}, t+\tau)$ and $\tilde{E}(\vec{r}, t)$ are uncorrelated, the phase of the function $\tilde{u}$ can take any value between 0 and 2π so averaging will give zero as a result.

$g_{11\tau}$ is the second expression of correlation (figure 3.1 II), quantifying how "similar" the field is at point $\vec{r}$ over a time window τ. It gives the level of longitudinal coherence over a time τ. For fully coherent fields $|g(\tau)| = 1$ while totally random fields produce $g(\tau) = 0$. Usually[36] one defines as *coherence time* the time interval, τ_c, over which $|g(\tau)|$ drops by a factor e, $|g(\tau_c)| = 1/e$. For an arbitrary source we have :

$$\tau_c = \int_{-\infty}^{\infty} |g(\tau)| d\tau. \tag{3.6}$$

Variations along t for a quasi monochromatic radiation beam, manifest in the frequency of the field. Over a time window T, the frequency content is given by $V_T(\nu) = \int_{-T/2}^{T/2} \tilde{E}(t) \exp(-i2\pi\nu t) dt$. The measurement accessible quantity in the frequency domain is the power spectral density or *spectrum*:

$$S(\nu) = \lim_{T\to\infty} \frac{1}{T} \langle |V_T(\nu)|^2 \rangle. \tag{3.7}$$

There is an intrinsic connection between the time and frequency domain for EM waves and it is expressed by the relation between the autocorrelation function $G(\tau)$ and the power spectral density $S(\nu)$:

$$S(\nu) = \int_{-\infty}^{\infty} G(\tau) \exp(-i2\pi\nu\tau) d\tau. \tag{3.8}$$

Equation 3.8 is known as the *Wiener-Kinchin* theorem[36] and offers a way to convert from spectral density to longitudinal coherence.

For well behaved, quasi-monochromatic lightsources, such as FELs, the spectral power is contained in a small region $\Delta\nu$ around a central frequency ν_0. The relation between the spectral width and the coherence time depends on the shape of the spectral profile. For example for a Gaussian profile, the relation between the full width at half maximum and the coherence time is $\Delta\nu_{FWHM} = 0.66/\tau_c$. There is a specific definition of the spectral width for which the function converting between spectral width and coherence time is independent of the shape of the spectrum:

$$\begin{aligned} \text{if } \Delta\nu_c &= \frac{\left(\int_0^\infty S(\nu)d\nu\right)^2}{\int_0^\infty S(\nu)^2 d\nu} \\ \text{then } 1/\tau_c &= \Delta\nu_c. \end{aligned} \tag{3.9}$$

Having a relation between the spectral width and the coherence time allows us to directly estimate longitudinal coherence of an EM pulse by studying its spectrum. For the studies in **paper III** and **IV** we use the spectral width as the measurement accessible quantity used to describe longitudinal coherence. In fact in **paper IV** we directly use the FEL spectra as the figure of merit for both longitudinal coherence and pulse power when comparing different schemes.

3.1.2 Transverse coherence

For points in the beam with no time delay, $\tau = 0$, the mutual coherence function transforms into the *mutual intensity* function that expresses the level of correlation in the beam between points $\vec{r}_1$ and $\vec{r}_2$ along the beam:

$$G_{120} = G(\vec{r}_1, \vec{r}_2) = \langle \tilde{E}(\vec{r}_1, t)\tilde{E}^*(\vec{r}_2, t)\rangle \tag{3.10}$$

$$g_{120} = g(\vec{r}_1, \vec{r}_2) = \frac{G(\vec{r}_1, \vec{r}_2)}{\sqrt{G(\vec{r}_1, \vec{r}_1, 0)G(\vec{r}_2, \vec{r}_2, 0)}}. \tag{3.11}$$

To obtained the normalized version of the mutual intensity function, we divide it by the square root of the product of the two averaged intensities at points $\vec{r}_1$ and $\vec{r}_2$ (equation 3.11). The normalized version, g_{120}, is called **complex degree of transverse coherence** and, as all other normalized quantities in this chapter, is bounded between 0 and 1 in its absolute value.

One can use the same approach to understand the g_{120} as for $g_{11\tau}$, where the variation of the phase of the product $\tilde{E}(\vec{r}_1, t)\tilde{E}^*(\vec{r}_2, t)$ is considered. For two points that oscillate in unison, the value of $|g(\vec{r}_1, \vec{r}_2)|$ approaches unity, while points entirely random oscillations to each other will produce a null value of this function.

g_{120} is the third expression of correlation, III in figure 3.1, and describes how coherent two points $\vec{r}_1$ and $\vec{r}_2$ are. However, its use is limited, as there are infinite many pairs $(\vec{r}_1, \vec{r}_2)$ in the wavefront. The transverse coherence of a beam can be fully described with a single number, that integrates the contributions from all points in the beam, called the **total degree of transverse coherence**, ζ:

$$\zeta = \frac{\int |G(\vec{r}_1, \vec{r}_2, 0)|^2 d\vec{r}_1 d\vec{r}_2}{\left(\int G(\vec{r}, \vec{r}, 0) d\vec{r}\right)^2}. \tag{3.12}$$

The quantity in equation 3.12 synthesizes, in a single number, the transverse coherence and is therefore the result of interest when measuring transverse coherence. It is the main figure of merit used in **paper III** to characterize the transverse coherence of FELs in both SASE[21,22] and HGHG configurations.

3.1.3 Cross-spectral density and total degree of coherence

A quasi-monochromatic source cannot have completely random fluctuations, therefore a representation in the frequency domain of the mutual coherence function is useful in characterizing sources with a very narrow bandwidth. Such a function is called the **cross spectral density** or CSD and it relates the fluctuations of the frequency component ν at points $\vec{r}_1$ and $\vec{r}_2$:

$$W(\vec{r}_1, \vec{r}_2, \nu) = \int_{-\infty}^{-\infty} G(\vec{r}_1, \vec{r}_2, \tau) e^{-i2\pi\nu\tau} d\tau. \tag{3.13}$$

We recall that fluctuations at different transverse points with a time delay τ are represented by $G_{12\tau}$. A Fourier Transform (FT) of $G_{12\tau}$ will thus result in the correlation of points $\vec{r}_1$ and $\vec{r}_2$ of each frequency component ν.

Using the substitution $\vec{r}_1 = \vec{r}_2 = \vec{r}$, $W(\vec{r}_1, \vec{r}_1, \nu) = S(\vec{r}, \nu)$, which is just the spectral density at position $\vec{r}$. As all quantities described before in this chapter, we also define a normalized version of CSD called **spectral degree of coherence**:

$$\mu_{12\nu} = \mu(\vec{r}_1, \vec{r}_2, \nu) = \frac{W(\vec{r}_1, \vec{r}_2, \nu)}{\sqrt{S(\vec{r}_1, \nu) S(\vec{r}_2, \nu)}}. \tag{3.14}$$

This quantity is also bounded between 0 and 1 and represents the coherence of the field points $\vec{r}_1$ and $\vec{r}_2$ at frequency ν.

We can define a frequency dependent ζ as:

$$\zeta(\nu) = \frac{\int |W(\vec{r}_1, \vec{r}_2, \nu)|^2 d\vec{r}_1 d\vec{r}_2}{\int |S(\vec{r}, \nu) d\vec{r}|^2}. \tag{3.15}$$

For quasi-monochromatic sources, such as FELs, which have a very narrow bandwith it may be enough to calculate $\zeta(\bar{\nu}) \equiv \zeta$, where $\bar{\nu}$ is the mean frequency component of the spectrum.

3.2 Transverse coherence in the Gauss Schell-model

The total degree of transverse coherence ζ is the goal figure of merit used to characterize any radiation sources. Due the FEL radiation's properties such as low divergence and quasi-monochromaticity we can use a simplifying model, the Gaussian Schell-model (GSM), to determine this value through, measurement accessible, quantities.

3.2.1 Propagation of CSD by mode decomposition

A partially coherent source can be represented as a superposition of fully coherent Gaussian modes[37]:

$$W(\vec{r}_1, \vec{r}_2, \nu) = \sum_j b_j \tilde{E}_j(\vec{r}_1, \nu) \tilde{E}_j^*(\vec{r}_2, \nu) \tag{3.16}$$

where b_j and $\tilde{E}_j$ are the eigen-value eigen-vector solutions to the equation :

$$b_j \tilde{E}_j(\vec{r}_2) = \int_{-\infty}^{\infty} W(\vec{r}_1, \vec{r}_2, \nu) \tilde{E}_j(\vec{r}_1) d\vec{r}_1.$$

A Gaussian beam with known electric field $E_j(\vec{r}, \nu; z)$ at the plane Σ can be analytically propagated through free space over a distance Z by:

$$E_j(\vec{r},\nu;z) = \int_\Sigma E_j(\mathbf{s},\nu)P_z(\vec{r}-\mathbf{s},\nu)d\mathbf{s} \tag{3.17}$$

with the Green's function propagator:

$$P_z(\vec{r}-\mathbf{s},\nu) = \frac{\nu}{icz}\exp\left[\frac{\pi\nu}{cz}(\vec{r}-\mathbf{s})^2\right].$$

Therefore the CSD, as the sum of these modes, is described at position $z = Z$ by:

$$W(\vec{r}_1,\vec{r}_2,\nu;z) = \sum_j b_j E_j(\vec{r}_1,\nu;z)E_j^*(\vec{r}_2,\nu;z). \tag{3.18}$$

This property is especially useful in propagating the CSD in space along the z direction perpendicular to the wavefront. As the value of the CSD is simply the sum of the propagated constituting modes.

3.2.2 Gauss Schell-model sources

The GSM is the most widely-used description of quasi-monochromatic sources such as FELs[20,21,38] when considering their coherence. In this model both the spectral intensity and the transverse coherence are assumed to have Gaussian shapes at the origin. Meaning that transverse coherence falls of as a Gaussian with distance. This shape remains constant with propagation through free space, thus allowing for a full characterization of a beam's coherence anywhere in space by performing measurements at any one position $z = Z$.

Furthermore, such sources' complex degree of transverse coherence g_{120} does not depend on the absolute positions $\vec{r}_1$ and $\vec{r}_2$ but rather on the distance between any two points $\Delta\vec{r} = \vec{r}_2 - \vec{r}_1$. GSM beams are described by a CSD of the type:

$$W_{GSM} = \sqrt{S_{GSM}(\vec{r}_1,\nu)S_{GSM}(\vec{r}_2,\nu)}\mu_{GSM}(\Delta\vec{r},\nu) \tag{3.19}$$

with the spectral intensity and complex degree of spatial coherence are have Gaussian dependence on the transverse coordinates x,y:

$$S_{GSM}(\vec{r}) = S_{0x}S_{0y}\exp\left(-\frac{r_x^2}{2\sigma_x^2} - \frac{r_y^2}{2\sigma_y^2}\right) \tag{3.20}$$

$$\mu_{GSM}(\Delta\vec{r}) = \exp\left(-\frac{\Delta r_x^2}{2l_{cx}^2} - \frac{\Delta r_y^2}{2l_{cy}^2}\right). \tag{3.21}$$

Here r_x and r_y are the x and y component of the vector $\vec{r}$, Δr_x and Δr_y are the x and y component of the vector $\Delta\vec{r}$. The source size in the x and y plane is given by σ_x and σ_y respectively and the spatial coherence information is encoded in the coherence lengths l_{cx} and l_{cy} (the length over which g_{120} drops by e) for the x and y directions. Since the FEL is usually elongated along the y direction, we allow for different sizes and coherence lengths in the two directions. In equation 3.19 and 3.20 we have used the subscript GSM to denote that these expressions are valid only in the GSM approximation, from here on we omit the subscript but it should be understood that we assume the Gaussian-Schell model valid.

For brevity reasons, we only show the derivation for the x direction but the exact same treatment can be carried out for y. The Rayleigh length for GSM beams for a source waist size of $\sigma_{0,x}$ and coherence length at the source $l_{c,x}$ is given by[39]:

$$z_R = \frac{\pi\sigma_{0,x}^2\nu}{c}\delta \qquad (3.22)$$
$$\text{with } \delta = \frac{l_{c,x}}{\sqrt{l_{c,x}^2 + \sigma_{0,x}^2}}.$$

Using the definition of the total degree of transverse coherence from equation 3.15 and with the expressions for S and μ from equation 3.20 we can write the explicit form of ζ for a GSM beam:

$$\zeta_x = \frac{\int exp\left(-\frac{x_2^2+x_1^2}{2\sigma_x^2}\right) exp\left(-\frac{(x_2-x_1)^2}{l_{cx}^2}\right) dx_1 dx_2}{\left(\int exp\left(-\frac{x^2}{2\sigma_x^2}\right) dx\right)^2} \qquad (3.23)$$

where x_1 and x_2 are any two points on the x axis. The denominator is simply a Gaussian, while for the numerator we use an integral table[40] to solve and obtain:

$$\zeta = \frac{q_x}{\sqrt{4+q_x^2}} \text{ with } q_x = \frac{l_{cx}}{\sigma_x}. \qquad (3.24)$$

In the GSM approximation the mode content determines the level of transverse coherence[22]. We can write the relative intensity of the eigenvalues of the Gaussian-Hermitian modes[41] of equation 3.16, b_j, in the x or y direction, as :

$$\frac{b_j}{b_0} = \left(\frac{1-\zeta_x}{1+\zeta_x}\right)^j \qquad (3.25)$$

with b_j the intensity of mode j and b_0 is the fundamental mode.

It can be shown [22] that q_x remains constant as the beam propagates along z. Therefore, if one obtains the value for the total degree of transverse coherence at a position z, it describes the beam at any point along its propagation in free space, from source to experiment. We have now found a way to obtain ζ by means measurement accessible quantities, the FEL radiation size and coherence length, which is what we aimed for at the beginning of this chapter.

Chapter 4

Numerical and experimental methods

As we have seen in the **chapter 3**, the transverse coherence of a light beam is completely described by the total degree of transverse coherence ζ. The longitudinal coherence, on the other hand, is accessible through the spectral power density, or spectrum, of the radiation. In this chapter we present the numerical and experimental methods, used in the attached papers, through which one can obtain ζ or the spectrum for FEL radiation.

4.1 Experimental methods to measure transverse coherence

We have previously shown that we can obtain the total degree of transverse coherence, ζ, if we can find the coherence length and the FEL spot size. In this section we will describe how, with a Young double-slit experiment, we can gain access to the coherence length.

4.1.1 The Young double-slit experiment

In 1801, Thomas Young demonstrated the principle of light interference by shining light through two narrow slits[a], and observing the two radiation waves interfere on a screen located after the slits. The periodic alternation of bright and dark fringes, also

[a] In the original experiment, Young did not use slits but rather a thin card so that light passing on one side of the card would interfere with light passing on the other side.

know as the interference pattern, was conclusive proof of the wave-like behaviour of light. Based on the distance between the slits and the screen and also the periodicity in the interference pattern Young even determined the wavelength of the incoming radiation.

In a Young double-slit experiment, the intensity pattern is generated by the interference of a small portion of the beam coming from a slit 1 with another small portion of the beam coming from a slit 2 (figure 4.1), ideally with no time delay between them. It is essentially the physical manifestation of the mutual intensity function G_{120}, (see equation 3.11). The bright and dark fringes are due to the light arriving at various positions on the screen from different distances, slits 1 and 2. This relative delay creates relative phase difference and thus the two beams either cancel or enhance each other based on the observing position on the screen.

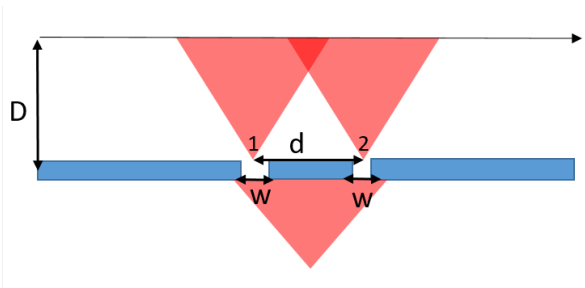

Figure 4.1: 1D schematic layout of Young double-slit experiment.

In the following, we will look at increasingly complex approximations of the interference patterns generated from a Young experiment. Our aim is to fit the experimental interference patterns to the theoretical ones so that we may extract the transverse degree of coherence, g_{120}, for each pattern. In this chapter we consider the slits placed along the x direction, for convenience, but any direction is treated similarly.

The first and simplest approximation is that of a fully coherent light beam. It has wavelength λ and passes through infinitely small slits, separated by a distance d. The intensity distribution along the x direction at distance D (see figure 4.1) from light shining through the slits is given by[36]:

$$I_{fit1}(\phi) = I_0[1 + \cos(\phi)]/2, \text{ with } \phi = \frac{2\pi x d}{\lambda D}. \tag{4.1}$$

The result in equation 4.1 can be extended[36] to account for a light beam with degree of transverse coherence $|g_{120}| < 1$. The interference pattern of this type of beam is given by:

$$I_{fit2}(\phi, |g_{120}|) = I_0[1 + |g_{120}| \cos(\phi)]/2. \tag{4.2}$$

A further extension of the interference pattern can be made if one takes into account the finite slit size w [42] is given by:

$$I_{fit3}(\phi, |g_{120}|) = I_0 \operatorname{sinc}\left(\frac{\phi w}{d}\right)[1 + |g_{120}| \cos(\phi)]/2. \tag{4.3}$$

The different fit functions I_{fit1}, I_{fit2} and I_{fit3}, and their envelopes, are plotted in figure 4.2. Depending on the level of accuracy needed from the approximation, one can use the different functions to fit a 1D double-slit interference pattern. The most realistic approximation, I_{fit3} from equation 4.3 is routinely used [43,44] to extract the complex degree of coherence from FEL radiation.

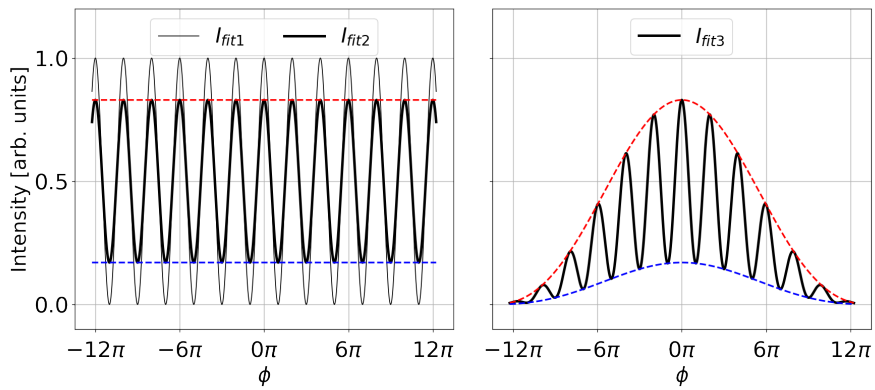

Figure 4.2: Plots of the different fitting functions used to approximate the Young 1D interference pattern. **left**: *black thin line* I_{fit1} fit function, *back thick line* I_{fit2} fit function, *blue dashed line*, lower envelope of I_{fit2} *red dashed line* upper envelope I_{fit2}; **right**: *back thick line* I_{fit3} fit function *blue dashed line*, lower envelope of I_{fit3} *red dashed line* upper envelope of I_{fit3}

4.1.2 FEL bandwidth and transverse coherence measurements

The picture of correlating the two points in the transverse plane of the EM field where the two slits are located, without any time delay, is only valid for the center point in the interference pattern. This point is situated at the same distance from slits 1 and 2 (at $\phi = 0$). As previously discussed, the interference pattern at other positions on the screen is influenced by the relative delay between the light beams coming from the two slits. This would not be of any concern if the radiation pulse had infinite

longitudinal coherence. However, for all "real" EM fields, such as FEL radiation, the *finite* coherence time can become significant if it is comparable in value to the relative delay at the observation point on the screen.

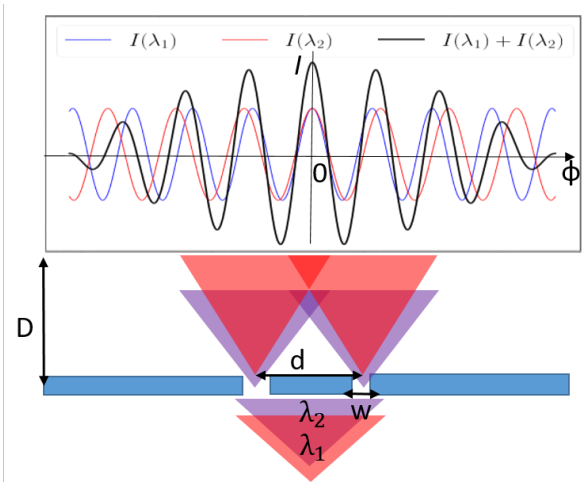

Figure 4.3: (Bottom): Schematic layout of the Young interference pattern. (Top): Interference pattern for light at two different wavelengths λ_1 (red), λ_2 (blue) and the combination of the two (black).

The effect of having two different wavelengths, λ_1 and λ_2, in a Young experiment is sketched in figure 4.3. Even if the radiation is coherent for each individual wavelength (red and blue lines), their combination (black line) will have a reduced visibility away from $\phi = 0$. Therefore, having a finite bandwidth of the light in a Young experiment means that fringe visibility is reduced at points on either side of the center of the interference pattern.

4.1.3 A fit function for the Fresnel region

Equation 4.3 is routinely used in FEL transverse coherence measurements[20,38,45] to fit the 1D intensity pattern by having the transverse degree of coherence as the free parameter. However, the equation is only valid for the far-field approximation, i.e., $\frac{w^2}{\lambda} \ll D$. Experimental setups in which $\frac{w^2}{\lambda} \approx D$ are said to be conducted in the **Fresnel** or near-field region[36] and thus, a more general fitting function has to be used.

To the best of our knowledge, there was no published closed form expression for the 1D interference patter from a Young double-slit experiment in the Fresnel region. In the appendix of **paper III** we derived such a closed form expression for a spherical wave incident on the slits. Here we present only the final result, the intensity as a function of position x on the CCD and distance z from the slits :

$$I_{fit}(x, z, |g_{120}|) = |A|^2[C_2^2 + C_1^2 + S_2^2 + S_1^2 + |g_{120}|(C_1C_2 + S_1S_2)] \quad (4.4)$$

with:

$$C_1 = C(w_{1,2}) - C(w_{1,1}) \; , \; S_1 = S(w_{1,2}) - S(w_{1,1}) \quad (4.5a)$$

$$C_2 = C(w_{2,2}) - C(w_{2,1}) \; , \; S_2 = S(w_{2,2}) - S(w_{2,1}). \quad (4.5b)$$

The functions C and S are the so called Fresnel integrals:

$$C(w) = \int_0^w \cos\left(\frac{ia^2}{2}\pi\right) da \; ; \; S(w) = \int_0^w \sin\left(\frac{ia^2}{2}\pi\right) da, \quad (4.6)$$

their values are tabulated and as *well-know* as, for example, the exponential function.

The explicit x and z dependence is found in the limits of integration $w_{i,j}$:

$$w_{1,1} = \sqrt{\frac{k(z_0 - z)}{zz_0\pi}} \left(\frac{-d}{2} - \frac{w}{2} - x\frac{z_0}{z_0 - z}\right) \quad (4.7a)$$

$$w_{1,2} = \sqrt{\frac{k(z_0 - z)}{zz_0\pi}} \left(\frac{-d}{2} + \frac{w}{2} - x\frac{z_0}{z_0 - z}\right) \quad (4.7b)$$

$$w_{2,1} = \sqrt{\frac{k(z_0 - z)}{zz_0\pi}} \left(\frac{d}{2} - \frac{w}{2} - x\frac{z_0}{z_0 - z}\right) \quad (4.7c)$$

$$w_{2,2} = \sqrt{\frac{k(z_0 - z)}{zz_0\pi}} \left(\frac{d}{2} + \frac{w}{2} - x\frac{z_0}{z_0 - z}\right) \quad (4.7d)$$

where z_0 is the position of the focus for the spherical wave and $k = 2\pi/\lambda$ is the radiation wavenumber.

We have, in the form of equation 4.4, a fit function for a Young experimental setup, valid also in the Fresnel region. The absolute value of the complex degree of coherence is thus accessible by fitting the experimental 1D interference pattern with the function in equation 4.4 (see figure 4.5).

4.1.4 Double-slit experiment at FERMI FEL-2

The aim of the double-slit experiment, presented in **paper III**, was to determine the total degree of transverse coherence ζ in equation 3.23 following these five steps :

1. Determine the FEL spot size $\sigma_{x,y}$ at the slits.

2. Measure intensity patterns for varying slit separations d.
3. Calculate the degree of transverse coherence g_{120} for each interference pattern.
4. Determine the coherence length $l_{c\,x,y}$ by fitting equation 3.21.
5. Calculate ζ from equation 3.24.

Out of the points outlined above, the most delicate one is the calculation of the degree of transverse coherence $|g_{120}|$ from the interference pattern and will therefore be the focus of this section. The intensity of the interfering fields from slit 1 and 2 is usually recorded by a 2D CCD grid (figure 4.4). The 1D interference pattern is obtained by taking the average along the y direction in the area highlighted in blue in figure 4.4, located at the maximum intensity.

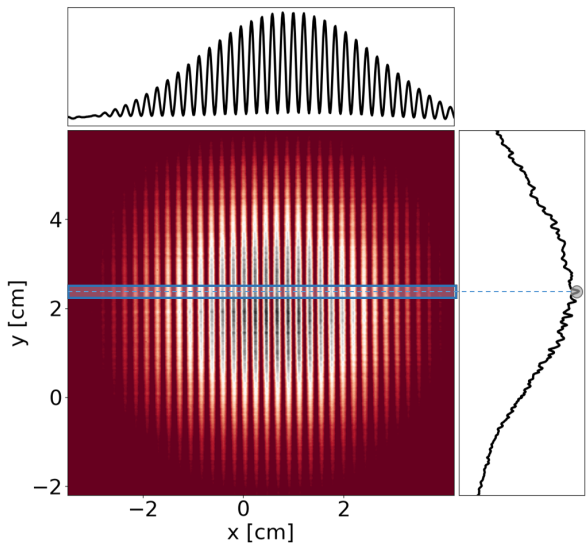

Figure 4.4: Measured 2D interference profile (bottom left), 1D y profile (right) and 1D interference pattern along x (top), obtained for the highlighted region (blue rectangle).

For the particular example of the experiment reported in **paper III**, the slit separation was varied between 0.4 and 1 mm, with a slit width of 40 μm for slit separations of 0.4, 0.5, 0.6 and 0.8 mm and 80 μm width for the 1 mm slit separation. The far-field criterion is not satisfied for all slits, therefore we had to use the fitting function valid in the near-field or Fresnel region (equation 4.4).

Figure 4.5 shows an example 1D interference pattern with unequal illumination of the two slits fitted by a modified version of equation 4.4. The unequal illumination here manifests by an oscillation of the minimum intensity at the position of the minima.

The unequal illumination can be accounted for in the fit function by multiplying the terms C_1 and S_1 in equation 4.4 with a scaling factor $f = I_1/I_2$ representing the relative difference in the radiation intensity coming from the two slits:

$$I(x, z, |g_{120}|) = |A|^2[f^2C_2^2 + C_1^2 + f^2S_2^2 + S_1^2 + |g_{120}|f(C_1C_2 + S_1S_2)]. \quad (4.8)$$

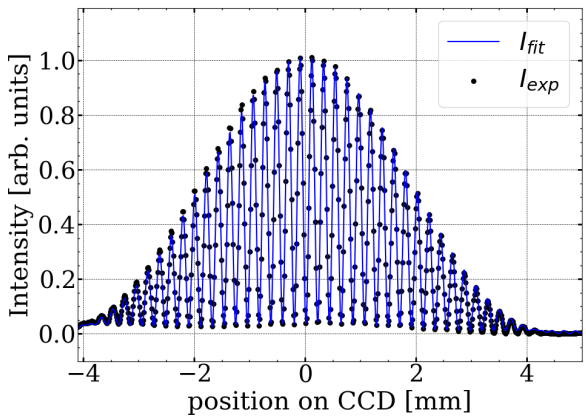

Figure 4.5: Example of 1D interference pattern (black dots) fitted with equation 4.8 (blue solid line)

4.2 Spectral analysis methods in characterizing temporal coherence

The relation between the spectral width, $\Delta\nu$, and coherence time, τ_c, has been described in **chapter 3** by equation 3.9. Furthermore, the investigation of longitudinal coherence by studying the radiation spectrum is a well established method[46,47,48]. In this section we detail a few ways of using the spectrum to estimate the coherence time and to detect coherence degradation effects.

3D FEL simulation codes such as Genesis 1.3[25] and FAST[49], offer the possibility to access the full 3D FEL radiation at predefined positions along the undulator. Numerous refinements and bench-marking processes have made Genesis 1.3 the standard FEL simulations tool. It is therefore easy to obtain the temporal profile of the radiation and from that, with a simple Fourier Transform (FT), the spectrum.

In measurements, the spectrum is usually acquired by placing a fine grating in the path of the light beam. The angle of scattering from the grating is wavelength dependent.

The scattered light is then detected on a photosensitive device (usually CCD), thus obtaining the wavelength dependent intensity or spectrum.

Electron beam longitudinal characterization is also an important tool in coherence studies. The FEL acts as an amplifier of the signals contained in the electron beam, therefore, strong features in the electron beam longitudinal profile will inevitably manifest themselves in the radiation spectrum.

At FEL machines, the electron longitudinal profile is usually obtained, with a transverse deflecting cavity[50] (TDC), which applies a time dependent angle deflection to the electrons in a bunch. Given enough propagation distance, the angle kick received by the electrons, will become a transverse offset at a viewing screen. The result is a density distribution of electrons, in the deflecting direction, based on their longitudinal position when passing through the cavity.

4.2.1 Spectrum along the beam in simulations

Using a particle tracking code such as ELEGANT[51] offers access to all the "macro-particle's" [b] positions and momenta. In this type of simulation environment, macroparticles are usually defined by their 6D vector (x, y, t, px, py, pz) consisting of positional (x, y, t) and momentum coordinates (px, py, pz). Hence, by using simulations, one has unfettered access to any profile of the electron beam.

Similar to the radiation intensity, one can apply the spectral analysis method to the beam current to reveal longitudinal density structures within the beam. We can calculate the particle density distribution along the beam as a function of t, i.e., a histogram, and Fourier transform it to obtain the bunching as a function of wavelength or *bunching spectrum*. This method is used in **paper IV** to investigate the change in bunching wavelength due to CSR, but it can also be used to study the microbunching gain during acceleration[52].

An interesting extension to this method is to define a bunching spectrum for different parts of the electron beam. Based on their longitudinal position (or any other criteria), one can select different regions and calculate their bunching spectra. For example in figure 4.6, we modulated the beam, in modulator 2 of an EEHG scheme, with slightly different amplitudes in the head (red) and tail (blue). We then looked at the bunching for the both individual regions (red and blue) and the entire bunch. We can see that only the amplitude used for the head creates bunching in the final beam.

This method of studying the bunching in different regions was used in **papers IV**,

[b] simulation codes usually do not simulate each electron, instead they use "macro-particles" that have the charge and mass of multiple electrons making computation times and memory requirements feasible.

V and VI because it allows for the detection of coherence ruining effects localized in specific regions of the bunch, without having to perform FEL simulations.

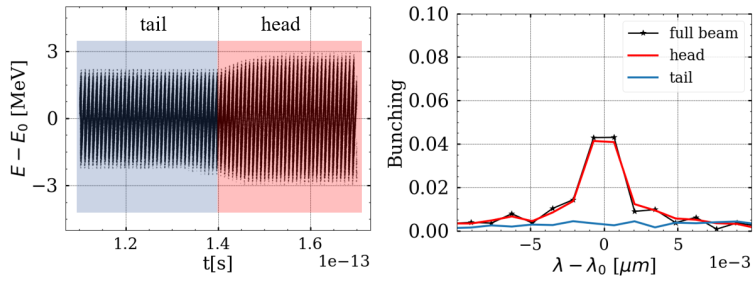

Figure 4.6: Right: Electron longitudinal phase space (black dots) split into head (red) and tail (blue) regions. Left: bunching spectrum for the head (red), tail (blue) and total (black with star) regions.

4.2.2 Peak detection in FEL radiation spectra

Certain phenomena acting on the electron beam, prior to arriving at the FEL radiators, can create micro-structures within it that hinder the FEL process. Small density modulations in the initial electron distribution created by the electron gun (or some other source) can be amplified by coherent synchrotron radiation inside the compressors. These density modulations can interfere with the seeding and FEL processes, decreasing longitudinal coherence and reducing the maximum power output[33,53].

To investigate this phenomenon we use the measured spectra and analyze its content more deeply. It is possible to find evidence for long wavelength modulations (orders of magnitude larger than the FEL radiation wavelength) by studying the separation of the individual peaks in the spectrum.

In **paper II**, a peak detection algorithm which allows for reliable detection of peaks above a certain intensity threshold is described. Then by analyzing the wavelength positions, of these peaks, one can infer the presence of modulations with certain wavelengths. In the example presented in figure 4.7 we concluded that a 6.3 μm period modulation is present in the electron beam.

Using the method described by (Roussel et al.)[54] one could imprint a known density modulation using a Laser heater at FERMI FEL-2. Figure 4.7 shows the FEL spectrum created by such a beam. Using the peak finding algorithm to fit spectrum we were able, based on the detected peaks position, to estimate the periodicity of the modulation in the electron beam.

Although this is preliminary work, it shows great potential for micro-bunching instability detection.

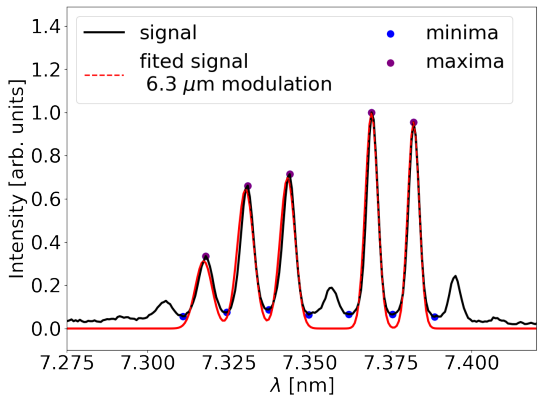

Figure 4.7: Example of peak detection with high threshold. Original signal (black line) fitted signal (red line), fitted minima (blue dots) and maxima (purple dots).

Chapter 5

Transverse coherence of SASE and seeded FELs

This chapter looks at the transverse coherence of seeded and SASE FELs to answer questions such as: How does transverse coherence evolve during the FEL process? And what can we learn form its sensitivity to electron beam parameters? We will answer these questions using experimental results, complemented by simulations and a semi-analytical approach.

5.1 Buildup of transverse coherence in FELs

Theoretical[55] investigations, simulations[56] and semi-analytical work[20] all indicate that transverse coherence of SASE FELs evolves during the FEL amplification process along the undulator. With the aim of comparing SASE and HGHG FELs in terms of transverse coherence, we conducted Young double-slit measurements at the FERMI FEL-2, operating the very same machine in SASE and cascaded HGHG modes.

5.1.1 Transverse coherence in simulations

Similar to the longitudinal mode selection, SASE amplification also "selects" transverse modes that dominate the (x, y) plane. Analytical work[20] and simulations[56] have shown, for SASE FELs, a clear dependence of the transverse coherence on the position along the power gain curve. However, there is no simple analytical expression for the evolution of transverse coherence along the undulator in the exponential

gain regime. Nevertheless, semi-analytical investigations [20,55] show that transverse coherence saturates earlier than FEL radiation power and can therefore be expected to reach its maximum value with fewer active undulators.

As mentioned in **chapter 4**, $3D$ FEL simulations are powerful tools for investigating the properties of the FELs radiation, giving access to the complex 3D radiation field at various stages of amplification. It is possible to obtain the total degree of transverse coherence, ζ, by applying equation 3.12 to the simulated field. Ding et al. [56] studied the SASE FEL at SLAC, using the Genesis 1.3 3D FEL simulation code. Their report also showed that saturation of the transverse coherence occurs earlier than power saturation.

By simulating the FERMI FEL-2, operated in SASE mode and applying the method from Ding et al. [56], but only in the x direction, we obtained the same trend of early saturation in transverse coherence buildup. The same method, applied for FERMI FEL-2 operated in cascaded HGHG mode, revealed an almost constant level for the ζ_x function. The variations of the normalized total degree of transverse coherence in the x plane with the position in the gain curve, of the two cases, are shown in figure 5.1. Here z_{sat} is the position where the FEL power saturates. The different transverse mode selection mechanisms are evidenced here by the different ζ_x trends of SASE and HGHG during the amplification process.

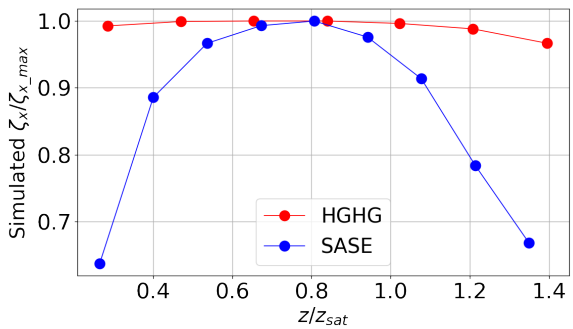

Figure 5.1: Normalized values for ζ_x in HGHG (red) and SASE (blue) simulations as a function of position in the power gain curve z/z_{sat}

These simulations suggest that the high transverse coherence associated with optical lasers is "transferred" to the FEL radiation through seeding. In SASE operations the dominant transverse mode seems to be selected out of the ones that independently form along the beam. This fact is apparent for the evolution of transverse coherence both before and after its maximum point, which suggests that once the dominant mode saturates, other modes become dominant.

5.1.2 Experimental comparison of transverse coherence in SASE and seeded FEL

Previous measurements at various FEL facilities[21,57], indicate that FEL radiation has relatively high levels of transverse coherence. However, a direct comparison between a SASE and a seeded FEL's transverse coherence properties was lacking. By using the FERMI FEL-2 facility (figure 5.2) with the identical electron beams, depicted in sub-figure 5.2-a, for both SASE and cascaded HGHG seeded operations, we could directly compare their transverse coherence. To the best of our knowledge, this was the first experimental observation of how transverse coherence is built up in SASE and HGHG FELs operated in the same setup.

Although the layout of FERMI FEL-2, presented in figure 5.2, was designed to function in a fresh-bunch cascaded HGHG mode (see figure 5.2-e), it can be easily changed to operate in SASE mode (figure 5.2-d) as well. By setting the resonant wavelength in the radiators of the first stage and in the modulator of the second stage to be the same as for the second stage radiators, i.e., 14.7 nm, one can use all these undulators in the SASE process, increasing the available magnetic length.

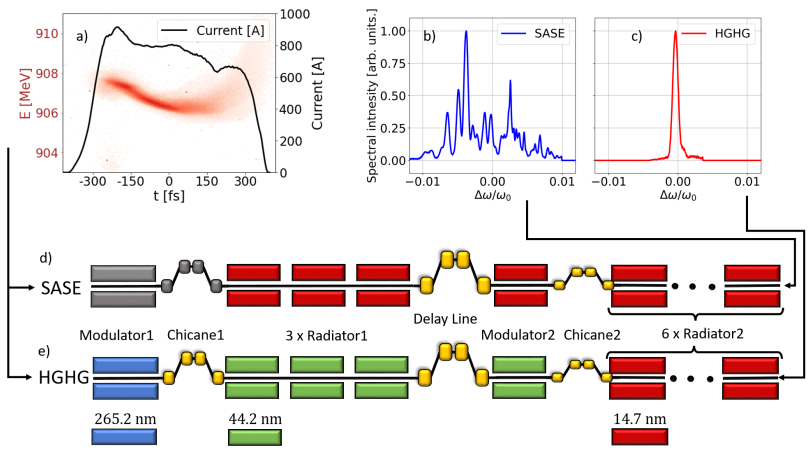

Figure 5.2: The FERMI-FEL-2 with a: the electron beam longitudinal phase space (red) with current (black line) at the entrance to the FEL, b: the experimental SASE spectrum, c: the experimental HGHG spectrum, d: the schematic layout of FERMI FEL-2 in SASE and e: the HGHG operation modes. Grey color on elements symbolizes they are not used. Undulator color codes specify the wavelength at which they were tuned.

By progressively tuning away undulators[a], in the radiator 2 part of the layout, we obtained snapshots of the FEL radiation with different numbers of active undulators. Since there is no interaction between the radiation and the electrons without the magnetic field of the undulators, tuning them out is equivalent to moving backwards in the FEL amplification process. For different number of active undulators we measured the energy of the FEL pulse, to establish the position along the power saturation gain curve, and transverse size, to use in ζ_x estimations.

For 4, 5 and 6 active undulators we introduced slits, of various separations, in the path of the radiation and recorded the interference pattern, as described in **chapter 4.1.1**. This set of measurements allowed us to determine the coherence length which, in combination with the field size yields, through equation 3.24, the total degree of transverse coherence for the x plane, i.e., ζ_x.

The evolution of ζ_x as a function of number of active undulators for SASE (blue) and HGHG (red) is presented in figure 5.3 (bottom). The correspondence to the position along the gain process is shown by plotting the FEL power as a function of active undulators. Analyzing the gain curves reveals that HGHG reaches power saturation with five undulators while SASE is still in the exponential amplification regime even using all the six undulators.

Analysis of the ζ_x trends shows that, in the case of HGHG, transverse coherence remains almost constant at all measurement points. On the other hand, for SASE, the transverse coherence reaches a saturation point with five active undulators. Correlating the gain curve results with the ζ_x trends demonstrates that, for SASE FELs, transverse coherence reaches a maximum before the pulse power saturation. Furthermore, these experimental results confirm all three characteristics discussed in relation to the simulation results of figure 5.1. First, SASE transverse coherence shows a strong dependence with the position in the gain curve. Secondly, SASE exhibits early saturation and finally, HGHG has an almost constant level of transverse coherence all through the gain process.

[a]In FEL gain curve measurements the gap of the undulators is usually opened so that the field inside the undulator almost disappears

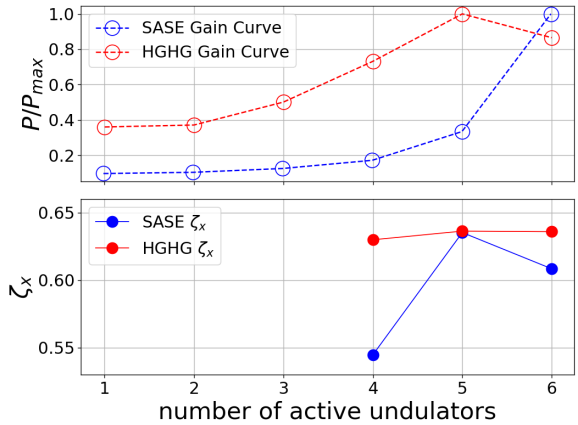

Figure 5.3: Top: Power Gain curve for SASE (blue) and HGHG (red). Bottom: evolution of total degree of transverse coherence, ζ_x, measured along the undulator for SASE (blue) and HGHG (red)

Both configurations reach similarly high values for the total degree of transverse coherence $\zeta_x \approx 0.64$. Using the mode decomposition approximation in **chapter 3.2.1**, a partially coherent source can be seen a superposition of fully coherent Gaussian modes. Given ζ_x, the relative intensity, b_i/b_0, of these modes is expressed in equation 3.25. For this experiment we found that $78\,\%$ of the power is in the fundamental b_0 mode and $18\,\%$ in the second b_1 mode.

The value $\zeta_x \approx 0.64$ is not as high as for "fully" coherent sources[37] and we can speculate about a couple of reasons why. It may be the case that there are some electron beam properties which limit the maximum achievable total degree of transverse coherence. Either some structure in the electron beam that not even seeding can overcome, or a mismatch between emittance and radiation diffraction size which we will address in the next section.

It is also possible, however, that we were limited in our estimations of the transverse coherence length, $l_{c,x}$, by the available slit separations. Our maximum slit size was $1\,\text{mm}$ and $l_{c,x} \approx 2\,\text{mm}$ for both SASE and HGHG. The errors in estimating ζ_x are larger if the range of available slit separations is smaller. Using the more accurate fitting function (equation 4.4), did help in this respect by providing better estimations of the transverse degree of coherence, g_{120}, for each slit separation, but it may not have been enough to compensate for their limited range.

Nevertheless, the conclusions of the experiment, in terms of the evolution of the total degree of transverse coherence, remain valid. Moreover, as both FELs reached similarly high maximum values of ζ_x, we can assume that the limitations, if any, did not

favour one mode of operation over the other and thus the comparison still stands.

5.2 Sensitivity of transverse coherence

Studying the sensitivity of transverse coherence w.r.t. electron beam properties can help more accurately pinpoint the mechanisms that create, but also the ones that distort this property of FEL radiation.

5.2.1 FEL bandwidth and transverse coherence measurements

The difference in bandwidth between SASE and HGHG (figure 5.2-b and c) could affect the estimations of the transverse degree of coherence, g_{120}, in measurements as described in chapter 4.1.2. We calculated the effect of finite wavelength bandwidth on the transverse coherence in two ways.

First, we considered no coupling between longitudinal and transverse coherence and assumed, according to the GSM, that both types of coherence obey a Gaussian decay law with time and distance respectively. By analyzing the spectra of the two beams we could find the coherence time, i.e., the time window τ over which the complex degree of longitudinal coherence $g_{11\tau} = 1/e$. Next, we calculated the time delay between the light coming from slits 1 and 2 at the edges of the CCD (where the delay is maximum). Comparing the coherence time and the maximum delay we could estimate that the bandwidth has an effect of roughly 2 % on the visibility of the fringes at the edges of the CCD. However, the central points in the interference pattern, which have more intensity, are weighted more in the fitting procedure and therefore the fitted g_{120} will be even less sensitive to this effect.

A second, more pragmatic approach, was to generate interference patterns for a distribution of wavelengths, with intensities for each wavelength given by the spectra of SASE and HGHG (figure 5.2-b and c respectively) and add them together. We then tried to fit the result with the Fresnel fit function (equation 4.4) and found a difference of 1 % in the estimated g_{120}.

Both approaches proved that, for this experiment, the influence of the bandwidth on the estimations of transverse coherence is negligible. However, it is difficult to completely remove the effect of longitudinal coherence in transverse coherence measurements. It may in fact be desirable to introduce a delay between the radiation coming from the two slits, in this way one could probe the more general, complex degree of coherence function, $g_{12\tau}$, to estimate a coherence "volume".

5.2.2 Transverse coherence and electron beam energy spread

We have seen in **chapter 2.4.2** that an increase in the electron energy spread, σ_γ, has the effect of increasing the gain length of the FEL. Thus, the FEL radiation power measured at the same fixed physical point in the undulator line, but for runs with different electron energy spread, will actually be measured at different number of gain lengths in the amplification process. One can therefore slightly "move" along the gain curve, while keeping the physical measurement point fixed, by changing the energy spread of the electrons.

By using a Laser heater (LH)[58], we were able to introduce controlled amounts of energy spread in the electron beam during our experiment at FERMI FEL-2. For certain values of induced energy spread we measured the FEL pulse's energy and the total degree of transverse coherence ζ_x.

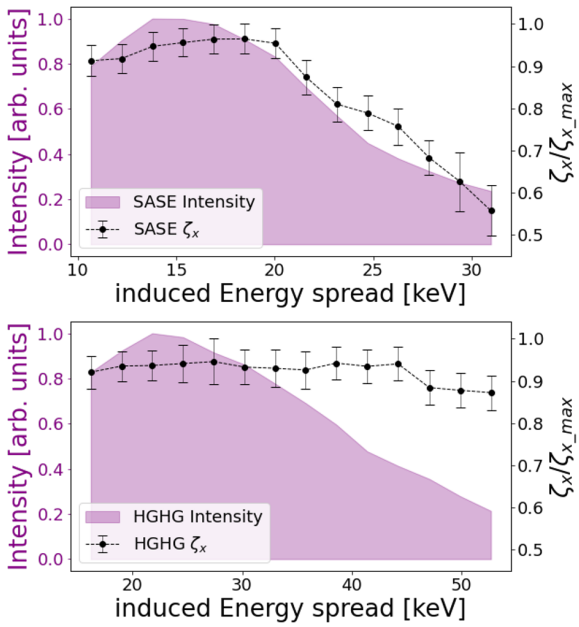

Figure 5.4: Evolution of FEL intensity (purple) and normalized total degree of transverse coherence, ζ_x, (black) with energy spread induced in the LH for SASE (top) and HGHG (bottom)

The dependence of the measured FEL radiation intensity on the induced energy spread (figure 5.4) tells us that two things. Firstly, that for large values of LH induced energy spread the FEL radiation intensity decreases considerably, supporting the picture of moving backwards in the gain curve by increasing electron energy spread. Secondly, that the highest FEL intensity is not at zero LH induced energy. We attribute the initial increase in FEL intensity with LH induced energy spread to the

suppression of micro-bunching instabilities[53,59] in the electron beam.

The transverse coherence of the HGHG FEL is shown (figure 5.4 black traces) to be independent of the induced energy spread, with variations at the level of the measurement uncertainties.

On the other hand, SASE's transverse coherence strongly depends on energy spread, dropping by 35 % at 30 keV induced energy spread, for the considered case. This effect indicates, yet again, that the SASE transverse coherence is highly dependent on the position in gain curve. Furthermore, since the maximum intensity of SASE occurs at lower energy spread values (at a later stage in the gain process) compared to the maximum of ζ_x, we also confirm the predictions that transverse coherence saturates faster than pulse power.

More experimental results, at various machines, involving other electron beam parameters are needed to complete the understanding of transverse coherence buildup. Nevertheless, it is clear that seeding an FEL ensures a high degree of coherence from the start while SASE FELs become more coherent as the FEL high-gain process unfolds.

5.2.3 Emittance influence on coherence

In the case of the transverse coherence experiment we performed at FERMI, the same beam was used in the two modes of operation. Based on emittance measurements, we determined $\epsilon_n = 2\,\text{mm·mrad}$.

According to Saldin et al.[20] a good matching between the radiation wavelength, λ_{rad}, and the beam emittance, can have a strong influence on the maximum achievable ζ (for both x and y directions) in an FEL. The condition for obtaining the maximum ζ value at saturation was shown to be: $\frac{2\pi\epsilon}{\lambda_{rad}} = 1$ or $\frac{\epsilon_n 2\pi}{\gamma\lambda_{rad}} = 1$. A possible interpretation of this peculiar effect is that a lower emittance allows for more independent transverse modes to form across the electron beam[55], thus limiting the maximum achievable transverse coherence.

Given $\gamma = 1757$ and $\lambda_{rad} = 14.7\,\text{nm}$, the electron beam emittance used in the experiment at FERMI was bellow the predicted, optimum value. This could indicate that the maximal attainable ζ, in both directions, was limited by the electron beam emittance in this experiment.

If we assume that the emittance is limiting the maximum transverse coherence, it is possible to view the emittance based effect as more fundamental to transverse coherence than whether the FEL is seeded or not. A more thorough investigation of the

dependence of ζ with emittance, for both SASE and seeded FELs, is needed in order to verify this assumption.

In terms of longitudinal effects, a FEL is considered to be seeded, if the "order" introduced by the seeding laser (or seeding technique) overcomes the randomness of "shot-noise". Based on the above discussion, one can speculate that, in order for a FEL to be seeded, in terms of transverse coherence, it must overcome the randomness in the *emittance* along the beam. This could be tested experimentally by creating a position dependent emittance profile in the electron beam. If one could reach a level of seeding for which, longitudinal coherence behaves like the FEL is seeded, while transverse coherence behaves like in a SASE FEL, then it would be apparent that there are different "seeding" thresholds for the longitudinal and transverse planes.

Chapter 6

Challenges and advantages of using EEHG seeding

During the last decade, EEHG based seeding techniques, have been proposed [60], studied [61,62] and experimentally demonstrated [15,16,63] at a number of FEL facilities around the world. The first proof of principle experiment [64] and later the first lasing at the 3^{rd} harmonic [15] were performed at the Stanford National Linear Accelerator (SLAC). The EEHG seeding technique has also been used at the Shanghai Deep Ultraviolet (SDUV-FEL) [65] and at FERMI FEL [16] to seed FELs at wavelengths as low as a few nm.

More advanced schemes using the original EEHG idea include, among other things, a staged layout which uses a double electron beam to achieve bunching at subnanometer wavelengths [18] and a storage ring FEL with the EEHG seeding option [66].

One of the advantages of EEHG seeding is its capability to generate bunching at high harmonics of the seeding laser which pushes the limit of the achievable wavelength in a seeded FEL. Another advantage is the scheme's robustness to jitter sources [16,60] compared to other seeding options.

The key to the high harmonics (short wavelengths) accessible through EEHG seeding is the creation of densely packed energy bands by the first, strong dispersive section. The first challenge we will address is the effect this strong dispersive section has on an electron beam with an linear profile in energy along the t coordinate, i.e., an *energy chirp*. We will show how the final phase space and current strongly depend on the combination of chirp and R_{56_1} signs.

The second challenge we will study is also related to the strong dispersive section. Due

to the strong magnetic fields required to reach the high values of R_{56_1}, significant levels of coherent synchrotron radiation (CSR) can be created (as seen in **chapter 2.6.1**). Furthermore, we show how it is possible to mitigate one of the effects of CSR using a specially tailored laser pulse profile.

6.1 Optimizing for EEHG seeding

In the following we will share some thoughts on how to choose the scaled parameters (A_i, B_i) and the integer n, in order to maximize the bunching level of EEHG. We will also take into account the energy spread in the final electron beam as well as collective effects due to strong magnetic fields in the first dispersive section, both of which can have significant effects on the EEHG FEL radiation.

The final bunching form of EEHG seeding is restated here for clarity:

$$b_{n,m} = \left| \exp\left[\frac{-1}{2}(\overbrace{nB_1 + aB_2}^{x})^2\right] J_m(-\overbrace{aA_2B_2}^{y}) J_n(-A_1 \overbrace{(nB_1 + aB2)}^{x}) \right| = \\ = \left| \underbrace{\exp(-x^2/2) J_n(A_1 x)}_{f_1} \underbrace{J_m(-y)}_{f_2} \right|. \tag{6.1}$$

In equation 6.1 we have defined two functions f_1, f_2 with arguments x, y respectively, to make it easier to identify the different components in the optimization process. The arguments x and y can be considered independent w.r.t. each other, since our original parameter space has five dimensions, enabling us to search for the maximum of f_1 and f_2 individually.

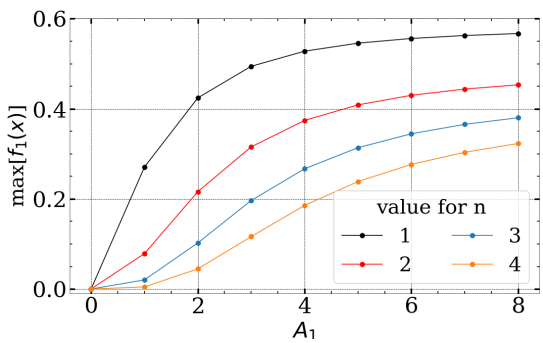

Figure 6.1: Dependence of the maximum attainable value of f_1 on the first modulation amplitude A_1

We start our analysis with the dependence of function f_1 on the order n and A_1, the first modulation amplitude. Numerical analysis on the maximum attainable value of of f_1, presented in figure 6.1, shows that selecting $|n| = 1$ offers a clear advantage. However, due to hardware limitations or constraints from effects such as CSR, it can be useful to select other values for n to reduce the value of B_1 as we shall see in the following. Using large values of A_1, essentially amounts to increasing the final energy spread of the electron beam, which means that a compromise must be made between the maximum of the function f_1 and the induced energy spread. Luckily, the trend presented in figure 6.1 shows the maximum value tapering off from values of $A_1 \geq 3$ for $|n| = 1$.

Optimizing function f_2 means finding the maximum value of a Bessel function of the first kind of a large order $m > 10$, which can be shown[34] to occur when the argument is:

$$y = aA_2B_2 \approx m + 0.81m^{1/3}. \tag{6.2}$$

For large values of m, the product $A_2 \cdot B_2 = y/a \approx 1$. One can reduce the value of A_2, which affects the final energy spread of the bunch, at the expense of increasing B_2. However we are further constrained in choosing the value of B_2 by f_1, which has global maximum at arguments $x \ll aB_2$. Therefore, one can estimate $B_1 \approx -aB_2/n$, which explains why choosing $|n| > 1$ can reduce the required value of B_1. The same relation tells us that, in order for B_1 and B_2 to have the same sign (for example using only chicanes in the EEHG scheme) n should be negative. The "good practices" rules in choosing A_2 and B_i can be summarized as:

$$A_2B_2 \approx 1 \tag{6.3a}$$

$$B_1 \approx -aB_2/n \tag{6.3b}$$

$$\text{for } m \gg n.$$

Equation 6.3 is useful in predicting the dispersive section strengths B_i given A_2, however, the exact choice of A_i and B_i is dependent on the available hardware at a specific machine. An optimization example for harmonic $a = 52$, used repeatedly in the following sections is presented in table 6.1. The compromise to have $A_1 < 3$ was made to reduce the final energy spread, while $A_2 = 4$ allows for a relatively low value of B_1 as $B_1 \approx -a/(nA_2)$.

Table 6.1: Example of EEHG scaled parameters for harmonic $a = 52$

A_1	A_2	B_1	B_2
2	4	13.3	0.27

6.2 The EEHG option for SXL and the challenge of a strong linear chirp

The MAX IV soft X-ray FEL (SXL) [19] is envisioned to deliver coherent, high intensity radiation to users in the $1 - 5$ nm wavelength range. The electron beam will be accelerated by the existing MAX IV LINAC to an energy of 3 GeV and compressed to peak currents of several kA using a double-achromat compression scheme [67]. As a way to improve longitudinal coherence, the EEHG seeding option has been considered for SXL as part of phase II [19]. The particular challenge of implementing EEHG at SXL comes from the high energy chirp present in the electron beam after acceleration and compression. Due to the fact that the final compression happens at full energy in the standard mode of operation, the residual chirp of the electron beam is around 0.5 MeV/fs.

If one is unable to remove the linear energy chirp of the electron beam prior to EEHG seeding, **paper I** indicates that, the sign of R_{56_1} should be chosen so that, in combination with the chirp sign, it compresses the electron beam. The reason for this is that such a combination generates an electron beam with higher current which increases the FEL radiation power. However, the higher peak current also means stronger coherent synchrotron radiation (see **chapter 2.6.1**), which can affect the quality of the bunching.

Two possibilities of EEHG seeding are considered for SXL. The first one involves placing the entire EEHG harmonic conversion scheme after the final bunch compressor (BC2) as shown in 6.2-b. A second option, which involves using the second Achromat of BC2 as part of the EEHG scheme, is shown in 6.2-c and was explored in paper V. We note here that because the R_{56} of Achromat 1 is opposite in sign to the "regular" Chicane 2, n should be positive, according to equation 6.3.

The existing bunch compressor is shown in figure 6.2-a, inside the dashed orange rectangle. It consists of two achromats with four dipoles each and an intrasection area marked by the blue dashed rectangles. To accommodate the two seeding options, the current layout figure 6.2-a needs to be modified.

In the first case, figure 6.2-b, two modulators and two Chicanes need to be added after Achromat 2 and before the radiators. This is the same standard EEHG layout as in figure 2.6-e. In the second case, figure 6.2-c, a modulator is placed between Achromats 1 and 2 and a single modulator and a Chicane is placed between Achromat 2 and the radiators. The idea behind the second option is to use the R_{56}, naturally present in Achromat 2, as the R_{56_1} in the EEHG technique. Along with providing a beam with higher peak current, the second option is also favoured from a design point of view. Not only does it need fewer new hardware components but, more

importantly, the extra space requirements between BC2 and the radiator line is just $4 - 5$ meters.

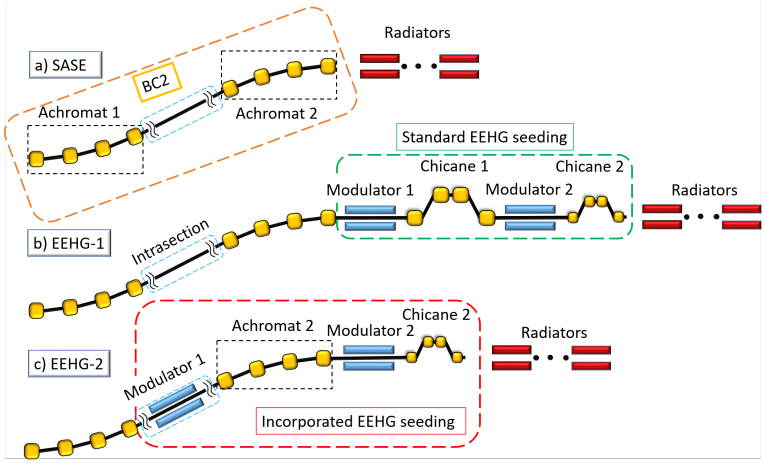

Figure 6.2: Schematic layout of SXL from BC2 to the radiators. a: for SASE operations b: for EEHG seeding after BC2 and c: EEHG seeding incorporated in BC2.

The results of operating SXL in SASE and the two EEHG seeding schemes are shown in figure 6.3. In SASE operation (figure 6.3-a) the beam is compressed to very high current ($\approx 4\,\mathrm{kA}$) and will produce radiation with $\Delta\lambda/\lambda = 1.7 \cdot 10^{-3}$ relative bandwidth. As the seeding cases are more sensitive to phase space distortions, the compression through the LINAC was slightly changed, to avoid collective effects due to high currents.

In the first seeding option, the beam will be stretched by the Chicane 1 because the electron energy chirp has the same sign as that of the Chicane R_{56_1}, resulting decompression (figure 6.3-b). This option produced the narrowest spectrum, as shown in figure 6.3. The second option produced a higher final current than the first option because its first dispersive section, Achromat 2, compresses the electron beam. However, there is some visible noise in its spectrum (figure 6.3-d, red line) which we attribute to CSR effects from BC2. Nevertheless, a 5 to 10 times narrowing of the spectrum is visible when comparing the spectra of the two EEHG seeding options with that of pure SASE. This proves that EEHG seeding can significantly increase longitudinal coherence for the SXL FEL.

The strong chirp of SXL can also affect the harmonic at which maximum bunching is obtained. As can be seen from figure 6.3-d, the two seeding options radiate at 4.9 and 5.1 nm which are harmonics 53 and 51 of the 260 nm seed laser. Even though there is, for both chirped beams, significant bunching at harmonic 52 (5 nm), the maximum bunching is at one harmonic down (EEHG-1) and one harmonic up (EEHG-2).

For comparison fairness, we picked the harmonic at which maximum bunching was obtained for both seeding cases, which is why they radiate at different harmonics.

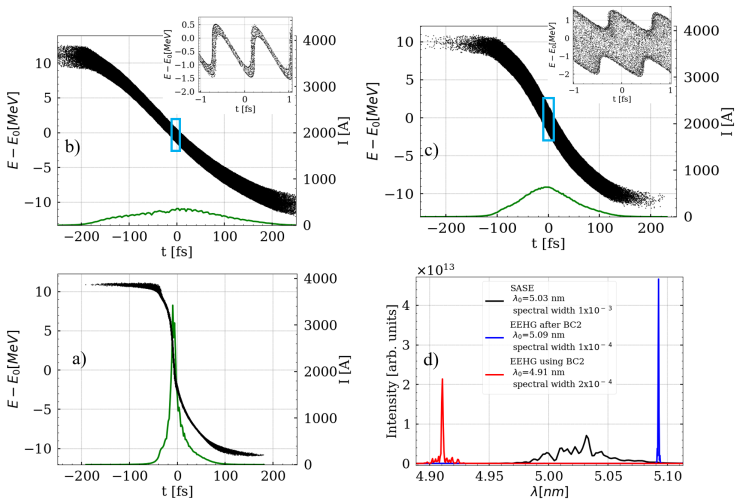

Figure 6.3: Electron phase space distributions (black dots) and current profiles (green lines) at the entrance to the radiators for a: SASE b: EEHG after BC2 and c: EEHG using BC2. d: FEL Spectrum for SASE (black), EEHG using BC2 (red) and EEHG after BC2 (blue).

Another interesting effect when implementing EEHG with a strong linear chirp is highlighted in the insets to figures 6.3-b and c, which represent a close-up of the final phase spaces using the two seeding schemes. Depending on the sign of the first dispersive section and that of the chirp, the width of the high current, high bunching regions, changes drastically. The width is determined by the number of energy modulation periods, produced by modulator 1, that are folded at the same longitudinal position ξ by DS1.

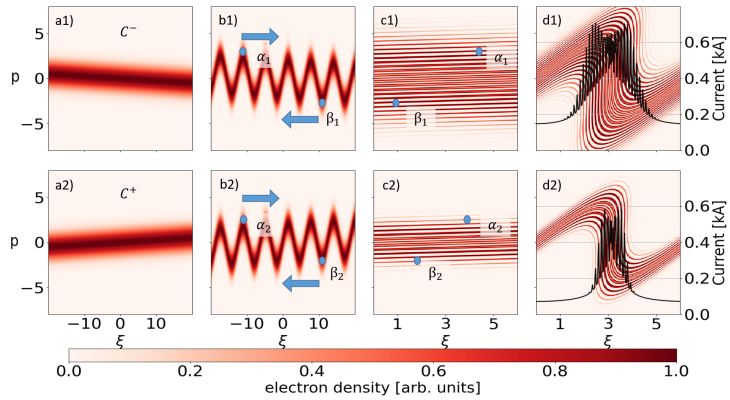

Figure 6.4: Phase space evolution through an EEHG seeding scheme of negatively (top) and positively (down) chirped electron beam. $a_{1,2}$ represents the initial phase spaces. $b_{1,2}$ the phase spaces after the first modulator. $c_{1,2}$ the phase spaces after the DS1. $d_{1,2}$ the phase spaces after the second DS and the beam current (black line).

To illustrate this phenomenon, we simulate the same principle, different combinations of R_{56_1} and chirp signs, but in the complementary case. If in the SXL case the chirp was fixed and we had two opposite signs of R_{56_1}, in the following we study the case of having the same R_{56_1}, but opposite chirps. In figure 6.4 we plot the phase space evolution in the two chirp cases, negative (top) and positive (bottom). After the modulation (plots $b1$ and $b2$), the two beams will pass through the DS1 which will fold the modulations on top of each other ($c1$ and $c2$). For this study, DS1 refers to the first Chicane but we use DS1 for consistency.

The different "folding" can be understood if we observe the effect the DS1 has on 4 different electrons, α_1 and β_1 for the negative chirp and α_2 and β_2 for the positive chirp. DS1 moves the particles along ξ based on their deviation in p, with positive deviations in p producing a positive displacement in ξ. Both α_1 and β_1 have larger energy deviations from $p = 0$ w.r.t their counterparts α_2 and β_2 and will therefore be displaced more. Following the 4 particles after DS1 (figure 6.4-c1 and c2), we can see that, for a negatively chirped beam, the particles are displaced more than for the positively chirped beam. The result is a higher number of energy bands in the phase space for the negative chirp, figure 6.4-c1, than of the positive chirp, figure 6.4-c2.

6.3 A possible solution to the challenge of CSR induced energy modulation

The sensitivity of the EEHG bunching to distortions in its phase space, has been explored in several studies[32,44,68]. Here we focus on the specific effect of bunching reduction due to coherent synchrotron radiation (CSR) in the first dispersive section (DS1) of the standard EEHG seeding scheme, presented in figure 2.6-e. We justify investigating this effect only in the first dispersive section (DS1) because, as we have seen in equation 6.3, the strength of the DS1 is tens of times larger than that of the DS2. Even though CSR has numerous effects on the electron beam, such as increased emittance and energy spread[29,31], we focus in the following on the long wavelength energy modulation imprinted on the electron beam, shown in figure 2.8. For this study we used the EEHG parameters described in table 6.1.

6.3.1 Long wavelength modulation

To visualize the CSR effect, we plot the longitudinal phase of the electron beam and the mean energy after the DS1 (figure 6.5-a). We designate "tail" and "head" to the distributions before and after 40 fs. As a first approximation, one can consider the energy modulation similar to imprinting two different chirps on the electron beam, one to the "tail" and one to the "head".

We have shown in **paper IV**, by making use of previous work[32], that introducing a linear chirp, $C = \frac{1}{E_0}\frac{dE}{cdt}$, between the first and second modulator, changes the final bunching wavelength $\Delta\lambda_h$ as:

$$\Delta\lambda_h = CR_{56\_2}\lambda_h. \tag{6.4}$$

Equation 6.4 implies that the differently chirped sections of the beam, will thus have, slightly different bunching wavelengths. To observe the change in bunching wavelength with chirp, we used the bunching spectrum along the beam, as described in **chapter 4.2.1**, applied to the final EEHG distribution. Figure 6.5-b shows that the two regions (head and tail), with different energy chirps, produce bunching at different wavelengths.

The mean energy profile, shown in figure 6.5-a, has strong resemblance to the CSR induced energy change in figure 2.8. This lends strength to our claim that the physical mechanism behind the "splitting" effect on the bunching is in fact CSR. Even though, for these simulations we choose EEHG parameters that require a lower R_{56_1} in the

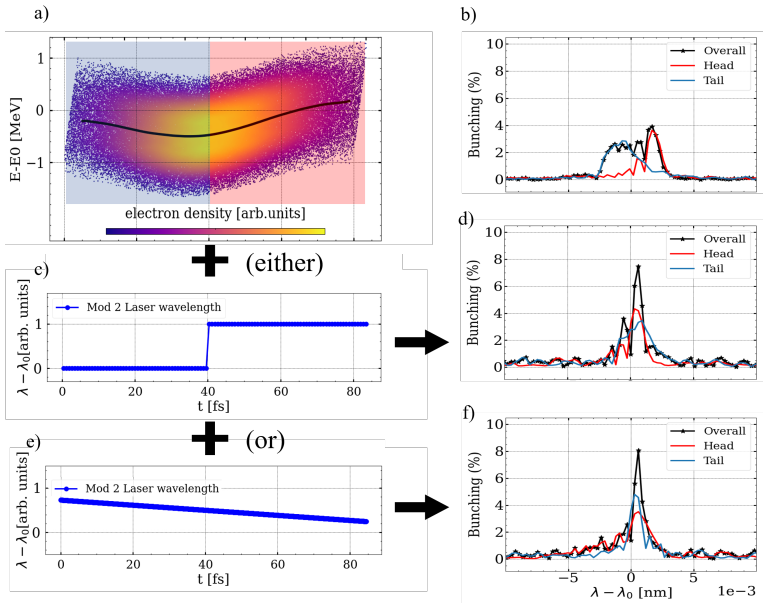

Figure 6.5: a: Electron beam phase space with head and tail highlighted in red and blue respectively. Mean slice energy (black line) b: bunching spectrum for the head (red), the tail (blue) and full beam (black) for constant wavelength of the laser in modulator 2. c: step wavelength profile of the laser in modulator 2 to compensate for CSR. d: bunching spectrum for the head (red), the tail (blue) and full beam (black) for wavelength profile in c. e: wavelength profile for a laser with a linear chirp in wavelength. f: bunching spectrum for the head (red), the tail (blue) and full beam (black) for wavelength profile in e.

DS1, reducing the CSR effect, it still has a significant impact on the bunching, which makes the investigation, and mitigation, all the more important.

6.3.2 Recovering bunching levels through tailor-made seeding laser profiles

The "splitting" of the bunching wavelength between the beam's head and tail will reduce the overall longitudinal coherence of the FEL radiation and it is therefore necessary to mitigate it. In **paper IV** we reported on this effect and proposed a solution to improve longitudinal coherence.

The analysis of bunching from the previous section, suggests that the way to compensate for the long wavelength CSR modulation is to find a parameter that can introduce a position dependent change in the final bunching wavelength. One such parameter is the wavelength of the seed laser in the second modulator. In an EEHG scheme, a "local" change of the second laser wavelength $\Delta\lambda_{mod\_2}$ will result in a proportional change of final bunching wavelength λ_h [44,69]:

$$\frac{\Delta\lambda_h}{\lambda_h} \approx \frac{\Delta\lambda_{mod\_2}}{\lambda_{mod\_2}}. \tag{6.5}$$

Therefore, if we modulate the two chirp regions of the electron beam with appropriately different λ_{mod_2}, we can recover the same bunching wavelength in the two regions. Indeed, figure 6.5-d shows that if one can create the correct wavelength *step* in the second seed laser, figure 6.5-c, the head and tail will bunch at the same wavelength.

The "structure" still visible in the bunching spectrum (figure 6.5-d) suggests that the picture of two linear chirps in the head and tail is an over-simplification of the energy profile. For a more accurate description, we need to consider a general energy dependence $E(t)$, which implies a general wavelength profile of the second seed laser, for compensation. We have shown, in **paper IV**, that to compensate for an energy profile of order n, a wavelength profile of order $n-1$ is appropriate:

$$\begin{aligned} &\frac{R_{56\_1}}{cE_0}\Big(\frac{dE}{dt} &&+\frac{d^2E}{dt^2}t + ...\Big) &&= \\ &\frac{1}{\lambda_{mod\_2}}\Big((\lambda_{mod\_2\_0} - \lambda_{mod\_2}) &&+\frac{d\lambda_{mod\_2}}{dt}t + ...\Big) \end{aligned} \tag{6.6}$$

Equation 6.6 shows the dependence between the energy profile, $E(t)$, of the electron beam and the wavelength profile, $\lambda(t)$, of the second modulator laser that compensates it. By isolating terms of the same order in t in equation 6.6, we can find a *linear* chirp in electron energy is compensated by a *shift* in wavelength, while for compensating a *quadratic* chirp, a *linear* chirp in wavelength is appropriate.

For this reason, we also tested compensating the energy profile seen figure 6.5-a, with a linear wavelength chirp (see figure 6.5-e). The results in figure 6.5-f show a slight improvement in the observable bunching structure with the new *linear* profile.

Analysis of the spectra from FEL simulations (figure 6.6) reveals that the longitudinal coherence of the radiation is improved when using either profile for the seed laser in modulator two. The bandwidth reduction when using a step and an linear wavelength profile is of 40 and 50 % respectively.

We conclude our investigations into this compensation method, with a short study on the effect of a laser jitter on the FEL spectra. Applying a small temporal offset to the laser profile of modulator two, we represent the effect of a timing jitter between the electron beam and the laser (figure 6.7).

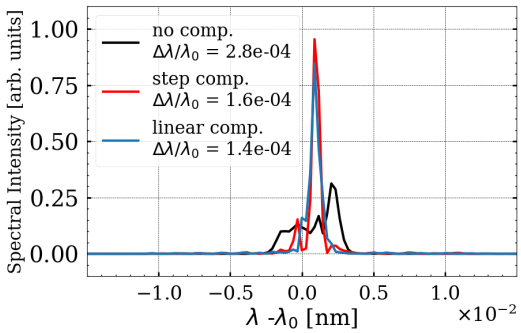

Figure 6.6: FEL spectra for the uncompensated case (back), the step in wavelength (red) and the linear chirp in wavelength (blue) profiles of the second seed laser.

A timing jitter will result, for the linearly chirped seed laser, in a shift of the central bunching, and subsequently FEL radiation wavelength. The cause of this shift can be understood by realizing that a long pulse, with a wavelength chirp C_{laser} measured with a delay Δt_{jit}, will simply have its wavelength shifted by $C_{laser} \cdot \Delta t_{jit}$.

On the other hand, a jitter in the step profile case results in a more complicated picture[a]. By delaying the laser w.r.t. the electron beam with Δt_{jit}, a portion of the electron beam, of the same duration Δt_{jit}, will be seeded by the wrong wavelength, giving rise to the familiar "splitting" observed in the uncompensated case.

Out of the two compensation methods, using a linear chirp for the laser profile is the more favourable for two reasons. It offers more resistance to timing jitter and, from the technical point of view, a linear wavelength chirp is by far easier to implement than a step function in the wavelength profile of a laser.

The study presented here and in **paper IV**, by means of simulations, opens the door to implementations in real machines of the considered compensation schemes. However, at a "real" FEL, choosing the correct chirp (or step) value in the laser wavelength would involve combining information about electron phase space and FEL spectrum. This analysis would be similar to the ones presented in **paper II**.

[a]for a more in-depth discussion the reader is referred to paper IV

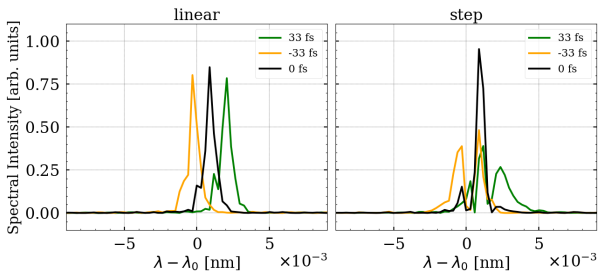

Figure 6.7: (left): FEL spectra for laser beam with linear wavelength chirp, in modulator 2, for delays of 33 fs (green), -33 fs (yellow) and no delay (black) (right): FEL spectra for a laser beam,in modulator 2, with a step function profile with delays of 33 fs (green), -33 fs (yellow) and no delay (black).

Chapter 7

Summary and Outlook

This thesis explores fundamental properties of FEL coherence through a dual, experimental and numerical, approach. After a theoretical description of the FEL process (**chapter 2**), I explained, in **chapter 3** the core concepts used to describe the coherence of EM radiation. I then described the numerical and experimental methods used to investigate coherence in FELs in **chapter 4** and presented the similarities and differences between SASE and seeded FELs' transverse coherence in **chapter 5**. **Chapter 6** contained work related to EEHG seeding as a method for improving longitudinal coherence and a solution for mitigating CSR effects on the EEHG scheme itself.

Free electron lasers have naturally high transverse coherence but, when investigating this property more closely, we found that, for seeded and SASE FELs, the process by which it is generated and maintained is fundamentally different. Furthermore, we experimentally verified that the power saturation point of SASE FEL does not coincide with the maximum in transverse coherence and that a HGHG seeded FEL has almost constant transverse coherence throughout the high gain regime.

The fact that seeded FELs have high transverse coherence from the start needs to be verified for other seeding schemes. Nevertheless, it does raise the question of what other, purposely introduced or not, features of the seed laser might also get amplified by the FEL process. This could lead the way to some novel shaping of the FEL radiation.

The intrinsic relation between spectral bandwidth and coherence time allows for investigation of the longitudinal coherence by analyzing the FEL radiation spectrum. The SASE FELs bandwidth i.e., $\Delta\nu/\nu = 10^{-3}$ can be improved by orders of magnitude through seeding. I studied the EEHG method of seeding from two perspectives: its implementation at the soft X-ray FEL (SXL) and the mitigation of CSR induced

effects due to the EEHG's strong first dispersive section.

The EEHG scheme was shown to significantly improve the bandwidth of the soft X-ray FEL, SXL. The challenges posed by the strong residual chirp in the SXL bunch were met with two seeding proposals. The first involves placing a standard EEHG setup between the LINAC and the FEL radiators while the second one utilizes half of the last bunch compressor as first dispersive section. The latter option reduces the space and hardware requirements and produces more radiation power by generating a beam with higher peak current. However, the spectral quality of the radiation can suffer from the increased coherent synchrotron radiation (CSR) because of the higher peak current.

Considering the CSR energy modulation as a varying energy chirp within the electron beam, we were able to better understand the reason for FEL spectral broadening and to come up with a way to mitigate it. As the "local" chirp changes so does the final bunching wavelength. By controlling the laser wavelength profile which seeds the electron beam in modulator 2, it is possible to compensate for the effect of varying chirp and increase the overall longitudinal coherence.

A natural continuation of this work will be to study the transverse coherence of EEHG seeded FELs as well as the influence of CSR on this property. Experimentally, this prospect is made feasible by the growing number of facilities considering EEHG seeding.

Another important avenue that could be pursued is to elaborate a streamlined procedure for transverse coherence measurements with online analysis. The spectral analysis and fitting codes can, with a proper optimization, be of great use in this endeavour. Making them available as online analysis tools would considerably improve the attainable quality of the FEL radiation.

References

[1] John M. J. Madey. Stimulated Emission of Bremsstrahlung in a Periodic Magnetic Field. *Journal of applied physics*, 42(February 1970):1906–1913, 1971. doi: https://doi.org/10.1063/1.1660466.

[2] Bela Adalbert Lengyel. *Lasers : generation of light by stimulated emission.* Wiley series in pure and applied optics. Wiley, 1962.

[3] R. Bonifacio, F. Casagrande, G. Cerchioni, L. de Salvo Souza, P. Pierini, and N. Piovella. Physics of the high-gain fel and superradiance. *La Rivista del Nuovo Cimento (1978-1999)*, 13(9):1–69, Sep 1990. ISSN 1826-9850. doi: 10.1007/BF02770850.

[4] A. M. Kondratenko and E. L. Saldin. Generation of coherent radiation by a relativistic electron beam in an ondulator. *Particle Accelerators*, 10(3-4):207–216, 1980. ISSN 0031-2460.

[5] A. Murokh et al. Measuring FEL Radiation Properties at VISA-FEL. In *Proc. PAC'01*. JACoW Publishing, Geneva, Switzerland, 2001.

[6] P Schmüser, M Dohlus, and J Rossbach. *Ultraviolet and Soft X-Ray Free-Electron Lasers: Introduction to Physical Principles, Experimental Results, Technological Challenges*. Springer, Berlin Heidelberg 2008, 2008. ISBN 978-3-540-79571-1. doi: 10.1001/archneurol.2012.1200.

[7] Oleg Yu. Gorobtsov, Giuseppe Mercurio, Flavio Capotondi, Petr Skopintsev, Sergey Lazarev, Ivan A. Zaluzhnyy, Miltcho B. Danailov, Martina Dell'Angela, Michele Manfredda, Emanuele Pedersoli, Luca Giannessi, Maya Kiskinova, Kevin C. Prince, Wilfried Wurth, and Ivan A. Vartanyants. Seeded x-ray free-electron laser generating radiation with laser statistical properties. *Nature Communications*, 9(1):4498, Oct 2018. ISSN 2041-1723. doi: 10.1038/s41467-018-06743-8.

[8] Christoph Bostedt, Sébastien Boutet, David M. Fritz, Zhirong Huang, Hae Ja Lee, Henrik T. Lemke, Aymeric Robert, William F. Schlotter, Joshua J. Turner, and Garth J. Williams. Linac coherent light source: The first five years. *Rev. Mod. Phys.*, 88:015007, Mar 2016. doi: 10.1103/RevModPhys.88.015007.

[9] Chi-Feng Huang, Wei-Hau Chang, Ting-Kuo Lee, Yasumasa Joti, Yoshinori Nishino, Takashi Kimura, Akihiro Suzuki, Yoshitaka Bessho, Tsung-Tse Lee, Mei-Chun Chen, Shun-Min Yang, Yeukuang Hwu, Shih-Hsin Huang, Po-Nan Li, Peilin Chen, Yung-Chieh Tseng, Che Ma, Tsui-Ling Hsu, Chi-Huey Wong, Kensuke Tono, Tetsuya Ishikawa, and Keng S. Liang. Xfel coherent diffraction imaging for weakly scattering particles using heterodyne interference. *AIP Advances*, 10(5):055219, 2020. doi: 10.1063/1.5129406.

[10] Tais Gorkhover, Anatoli Ulmer, Ken Ferguson, Max Bucher, Filipe R N C Maia, Johan Bielecki, Tomas Ekeberg, Max F Hantke, Benedikt J Daurer, Carl Nettelblad, Jakob Andreasson, Anton Barty, Petr Bruza, Sebastian Carron, Dirk Hasse, Jacek Krzywinski, Daniel S D Larsson, Andrew Morgan, Kerstin Mühlig, Maria Müller, Kenta Okamoto, Alberto Pietrini, Daniela Rupp, Mario Sauppe, Gijs van der Schot, Marvin Seibert, Jonas A Sellberg, Martin Svenda, Michelle Swiggers, Nicusor Timneanu, Daniel Westphal, Garth Williams, Alessandro Zani, Henry N Chapman, Gyula Faigel, Thomas Möller, Janos Hajdu, and Christoph Bostedt. Femtosecond X-ray Fourier holography imaging of free-flying nanoparticles. *Nature Photonics*, 12:150–153, 2018. ISSN 1749-4893. doi: 10.1038/s41566-018-0110-y.

[11] J Amann, W Berg, V Blank, F.-J. Decker, Y Ding, P Emma, Y Feng, J Frisch, D Fritz, J Hastings, Z Huang, J Krzywinski, R Lindberg, H Loos, A Lutman, H.-D. Nuhn, D Ratner, J Rzepiela, D Shu, Yu. Shvyd'ko, S Spampinati, S Stoupin, S Terentyev, E Trakhtenberg, D Walz, J Welch, J Wu, A Zholents, and D Zhu. Demonstration of self-seeding in a hard-X-ray free-electron laser. *Nature Photonics*, 6(10):693–698, 2012. ISSN 1749-4893. doi: 10.1038/nphoton.2012.180.

[12] L.-H. Yu, M. Babzien, I. Ben-Zvi, L. F. DiMauro, A. Doyuran, W. Graves, E. Johnson, S. Krinsky, R. Malone, I. Pogorelsky, J. Skaritka, G. Rakowsky, L. Solomon, X. J. Wang, M. Woodle, V. Yakimenko, S. G. Biedron, J. N. Galayda, E. Gluskin, J. Jagger, V. Sajaev, and I. Vasserman. High-gain harmonic-generation free-electron laser. *Science*, 289(5481):932–934, 2000. ISSN 00368075, 10959203.

[13] J. Bödewadt et al. sFLASH - First Results of Direct Seeding at Flash. In *Proc. LINAC'10*, pages 419–421. JACoW Publishing, Geneva, Switzerland, 2010.

[14] G. Stupakov. Using the beam-echo effect for generation of short-wavelength radiation. *Phys. Rev. Lett.*, 102:074801, Feb 2009. doi: 10.1103/PhysRevLett.102.074801.

[15] D. Xiang, E. Colby, M. Dunning, S. Gilevich, C. Hast, K. Jobe, D. McCormick, J. Nelson, T. O. Raubenheimer, K. Soong, G. Stupakov, Z. Szalata, D. Walz, S. Weathersby, M. Woodley, and P.-L. Pernet. Demonstration of the echo-enabled harmonic generation technique for short-wavelength seeded free electron lasers. *Phys. Rev. Lett.*, 105:114801, Sep 2010. doi: 10.1103/PhysRevLett.105.114801.

[16] Primož Rebernik Ribič, Alessandro Abrami, Laura Badano, Maurizio Bossi, Hans-Heinrich Braun, Niky Bruchon, Flavio Capotondi, Davide Castronovo, Marco Cautero, Paolo Cinquegrana, Marcello Coreno, Marie Emmanuelle Couprie, Ivan Cudin, Miltcho Boyanov Danailov, Giovanni De Ninno, Alexander Demidovich, Simone Di Mitri, Bruno Diviacco, William M Fawley, Chao Feng, Mario Ferianis, Eugenio Ferrari, Laura Foglia, Fabio Frassetto, Giulio Gaio, David Garzella, Amin Ghaith, Fabio Giacuzzo, Luca Giannessi, Vanessa Grattoni, Sandi Grulja, Erik Hemsing, Fatma Iazzourene, Gabor Kurdi, Marco Lonza, Nicola Mahne, Marco Malvestuto, Michele Manfredda, Claudio Masciovecchio, Paolo Miotti, Najmeh S Mirian, Ivaylo Petrov Nikolov, Giuseppe Maria Penco, Gregory Penn, Luca Poletto, Mihai Pop, Eduard Prat, Emiliano Principi, Lorenzo Raimondi, Sven Reiche, ElÃ©onore Roussel, Roberto Sauro, Claudio Scafuri, Paolo Sigalotti, Simone Spampinati, Carlo Spezzani, Luca Sturari, Michele Svandrlik, Takanori Tanikawa, Mauro TrovÃ³, Marco Veronese, Davide Vivoda, Dao Xiang, Maurizio Zaccaria, Dino Zangrando, Marco Zangrando, and Enrico Massimiliano Allaria. Coherent soft X-ray pulses from an echo-enabled harmonic generation free-electron laser. *Nature Photonics*, 13(8):555–561, aug 2019. ISSN 1749-4893. doi: 10.1038/s41566-019-0427-1.

[17] Erik Hemsing, Michael Dunning, Bryant Garcia, C. Hast, Tor O. Raubenheimer, Gennady Stupakov, and Dao Xiang. Echo-enabled harmonics up to the 75th order from precisely tailored electron beams. *Nature Photonics*, 10:512–515, 2016. doi: 10.1038/nphoton.2016.101.

[18] Zhentang Zhao, Chao Feng, Jianhui Chen, and Zhen Wang. Two-beam based two-stage eehg-fel for coherent hard x-ray generation. *Science Bulletin*, 61(9):720–727, 2016. ISSN 2095-9273. doi: https://doi.org/10.1007/s11434-016-1060-8.

[19] Weilun Qin, Francesca Curbis, Joel Andersson, Vitaliy Goryashko, Lennart Isaksson, Billy Kyle, Filip Lindau, Erik Mansten, Mihai Pop, Peter Salén,

Hamed Tarawneh, Pedro F. Tavares, Sara Thorin, Alexey Vorozhtsov, and Sverker Werin. The FEL in the SXL project at MAX IV. *Journal of Synchrotron Radiation*, 28(3):707–717, May 2021. doi: 10.1107/S1600577521003465.

[20] E L Saldin, E A Schneidmiller, and M V Yurkov. Statistical and coherence properties of radiation from x-ray free-electron lasers. *New Journal of Physics*, 12 (3):35010, 2010. doi: https://doi.org/10.1088/1367-2630/12/3/035010.

[21] A. Singer, F. Sorgenfrei, A. P. Mancuso, N. Gerasimova, O. M. Yefanov, J. Gulden, T. Gorniak, T. Senkbeil, A. Sakdinawat, Y. Liu, D. Attwood, S. Dziarzhytski, D. D. Mai, R. Treusch, E. Weckert, T. Salditt, A. Rosenhahn, W. Wurth, and I. A. Vartanyants. Spatial and temporal coherence properties of single free-electron laser pulses. *Opt. Express*, 20(16):17480–17495, Jul 2012. doi: 10.1364/OE.20.017480.

[22] I A Vartanyants and A Singer. Coherence properties of hard x-ray synchrotron sources and x-ray free-electron lasers. *New Journal of Physics*, 12(3):035004, mar 2010. doi: 10.1088/1367-2630/12/3/035004.

[23] John David Jackson. *Classical electrodynamics; 3rd ed.* Wiley, New York, NY, 1999.

[24] S. I. Bajlekov, W. M. Fawley, C. B. Schroeder, R. Bartolini, and S. M. Hooker. Simulation of free-electron lasers seeded with broadband radiation. *Phys. Rev. ST Accel. Beams*, 14:060711, Jun 2011. doi: 10.1103/PhysRevSTAB.14.060711.

[25] S. Reiche. Genesis 1.3: a fully 3d time-dependent fel simulation code. *Nuclear Instruments and Methods in Physics Research Section A: Accelerators, Spectrometers, Detectors and Associated Equipment*, 429(1):243 – 248, 1999. ISSN 0168-9002. doi: https://doi.org/10.1016/S0168-9002(99)00114-X.

[26] Helmut Wiedemann. *Particle accelerator physics*. Springer International Publishing Switzerland, 2015. ISBN 978-3-319-18316-9. doi: 10.1007/978-3-319-18317-6.

[27] Ming Xie. Exact and variational solutions of 3d eigenmodes in high gain fels. *Nuclear Instruments and Methods in Physics Research Section A: Accelerators, Spectrometers, Detectors and Associated Equipment*, 445(1):59–66, 2000. ISSN 0168-9002. doi: https://doi.org/10.1016/S0168-9002(00)00114-5.

[28] Sven Ackermann, Bart Faatz, and Velizar Miltchev. Modal analysis of a seeded free-electron laser. *Phys. Rev. ST Accel. Beams*, 16:100702, Oct 2013. doi: 10.1103/PhysRevSTAB.16.100702.

[29] E.L. Saldin, E.A. Schneidmiller, and M.V. Yurkov. Analytical treatment of the radiative interaction of electrons in a bunch passing a bending magnet. *Nuclear*

Instruments and Methods in Physics Research Section A: Accelerators, Spectrometers, Detectors and Associated Equipment, 407(1):112–115, 1998. ISSN 0168-9002. doi: https://doi.org/10.1016/S0168-9002(97)01378-8.

[30] E. L. Saldin, E. A. Schneidmiller, and M.V. Yurkov. Radiative interaction of electrons in a bunch moving in an undulator. *Nuclear Instruments and Methods in Physics Research Section A: Accelerators, Spectrometers, Detectors and Associated Equipment*, 417(1):158–168, 1998.

[31] A D Brynes, P Smorenburg, I Akkermans, E Allaria, L Badano, S Brussaard, M Danailov, A Demidovich, G De Ninno, D Gauthier, G Gaio, S B Van Der Geer, L Giannessi, M J De Loos, N S Mirian, G Penco, P Rebernik, F Rossi, I Setija, S Spampinati, C Spezzani, M Trovò, P H Williams, and S Di Mitri. Beyond the limits of 1D coherent synchrotron radiation. *New Journal of Physics*, 20(7):73035, 2018. ISSN 1367-2630. doi: 10.1088/1367-2630/aad21d.

[32] Erik Hemsing. Minimum spectral bandwidth in echo seeded free electron lasers. *Frontiers in Physics*, 7:35, 2019. ISSN 2296-424X. doi: 10.3389/fphy.2019.00035.

[33] E. Allaria, D. Castronovo, P. Cinquegrana, P. Craievich, M. Dal Forno, M. B. Danailov, G. D'Auria, A. Demidovich, G. De Ninno, S. Di Mitri, B. Diviacco, W. M. Fawley, M. Ferianis, E. Ferrari, L. Froehlich, G. Gaio, D. Gauthier, L. Giannessi, R. Ivanov, B. Mahieu, N. Mahne, I. Nikolov, F. Parmigiani, G. Penco, L. Raimondi, C. Scafuri, C. Serpico, P. Sigalotti, S. Spampinati, C. Spezzani, M. Svandrlik, C. Svetina, M. Trovo, M. Veronese, D. Zangrando, and M. Zangrando. Two-stage seeded soft-X-ray free-electron laser. *Nature Photonics*, 7(11):913–918, 2013. ISSN 1749-4885. doi: 10.1038/nphoton.2013.277.

[34] Dao Xiang and Gennady Stupakov. Echo-enabled harmonic generation free electron laser. *Phys. Rev. ST Accel. Beams*, 12:030702, Mar 2009. doi: 10.1103/PhysRevSTAB.12.030702.

[35] Milton Abramowitz and Stegun Irene. *Handbook of Mathematical Functions, With Formulas, Graphs, and Mathematical Tables,*. Dover Publications, Inc., USA, 1972. ISBN 0486612724.

[36] Bahaa EA Saleh and Malvin Carl Teich. *Fundamentals of photonics*. John Wiley & sons, 207.

[37] Leonard Mandel and Emil Wolf. *Optical Coherence and Quantum Optics*. Cambridge University Press, 1995.

[38] Evgeny Alexanrdovich Schneidmiller and M V Yurkov. Coherence properties of the radiation from FLASH. *Journal of Modern Optics*, 63(4):293–308, 2016.

[39] Greg Gbur and Emil Wolf. The rayleigh range of gaussian schell-model beams. *Journal of Modern Optics*, 48(11):1735–1741, 2001. doi: 10.1080/09500340108231429.

[40] I. S. Gradshteyn and I. M. Ryzhik. *Table of integrals, series, and products*. Elsevier/Academic Press, Amsterdam, seventh edition, 2007. ISBN 978-0-12-373637-6; 0-12-373637-4.

[41] F. Gori. Mode propagation of the field generated by collett-wolf schell-model sources. *Optics Communications*, 46(3):149–154, 1983. ISSN 0030-4018. doi: https://doi.org/10.1016/0030-4018(83)90266-3.

[42] B. J. Thompson and E. Wolf. Two-beam interference with partially coherent light. *J. Opt. Soc. Am.*, 47(10):895–902, Oct 1957. doi: 10.1364/JOSA.47.000895.

[43] J. Schwenke, N. Cutic, F. Lindau, S. Werin, and E. Mansten. Transverse Coherence and Polarization Measurement of Coherent Femtosecond Pulses from a Seeded FEL. In *Proc. FEL'11*, pages 458–460. JACoW Publishing, Geneva, Switzerland, 2011.

[44] D Ratner, A Fry, G Stupakov, and W White. Laser phase errors in seeded free electron lasers. *Physical Review Special Topics-Accelerators and Beams*, 15(3): 030702, 2012.

[45] S. Roling, B. Siemer, M. Wöstmann, H. Zacharias, R. Mitzner, A. Singer, K. Tiedtke, and I. A. Vartanyants. Temporal and spatial coherence properties of free-electron-laser pulses in the extreme ultraviolet regime. *Phys. Rev. ST Accel. Beams*, 14:080701, Aug 2011. doi: 10.1103/PhysRevSTAB.14.080701.

[46] Sven Ackermann, Bart Faatz, Vanessa Grattoni, Mehdi Mohammad Kazemi, Tino Lang, Christoph Lechner, Georgia Paraskaki, Johann Zemella, Gianluca Geloni, Svitozar Serkez, Takanori Tanikawa, and Wolfgang Hillert. Novel method for the generation of stable radiation from free-electron lasers at high repetition rates. *Phys. Rev. Accel. Beams*, 23:071302, Jul 2020. doi: 10.1103/PhysRevAccelBeams.23.071302.

[47] Luca Giannessi, Enrico Allaria, Laura Badano, D Castronovo, Paolo Cinquegrana, Paolo Craievich, Miltcho Danailov, G auria, Alexander Demidovich, G Ninno, S. Di Mitri, B. Diviacco, W Fawley, Eugenio Ferrari, Lea Fröhlich, Giulio Gaio, R Ivanov, Emanuel Karantzoulis, B Mahieu, and Marco Zangrando. First lasing of fermi fel-2 (1° stage) and fermi fel-1 recent results. In *FEL 2012 - 34th International Free Electron Laser Conference*, Geneva, Switzerland, 2012. JACoW Publishing.

[48] NR Thompson, DJ Dunning, and BWJ McNeil. Improved temporal coherence in sase fels. *Ipac2010*, pages 2257–2259, 2010.

[49] E. L. Saldin, E. A. Schneidmiller, and M. V. Yurkov. FAST: Three-dimensional time dependent FEL simulation code. *Nucl. Instrum. Meth. A*, 429:233–237, 1999. doi: 10.1016/S0168-9002(99)00110-2.

[50] D. Ratner, C. Behrens, Y. Ding, Z. Huang, A. Marinelli, T. Maxwell, and F. Zhou. Time-resolved imaging of the microbunching instability and energy spread at the linac coherent light source. *Phys. Rev. ST Accel. Beams*, 18:030704, Mar 2015. doi: 10.1103/PhysRevSTAB.18.030704.

[51] Michael Borland. Elegant: A flexible sdds-compliant code for accelerator simulation. Technical report, Argonne National Lab., IL (US), 2000.

[52] A. D. Brynes, I. Akkermans, E. Allaria, L. Badano, S. Brussaard, G. De Ninno, D. Gauthier, G. Gaio, L. Giannessi, N. S. Mirian, G. Penco, G. Perosa, P. Rebernik, I. Setija, S. Spampinati, C. Spezzani, M. Trovò, M. Veronese, P. H. Williams, A. Wolski, and S. Di Mitri. Characterisation of microbunching instability with 2d fourier analysis. *Scientific Reports*, 10(1):5059, Mar 2020. ISSN 2045-2322. doi: 10.1038/s41598-020-61764-y.

[53] S. Di Mitri and S. Spampinati. Microbunching instability study in a linac-driven free electron laser spreader beam line. *Phys. Rev. Accel. Beams*, 20:120701, Dec 2017. doi: 10.1103/PhysRevAccelBeams.20.120701.

[54] Eléonore Roussel, Enrico Allaria, Miltcho Danailov, Simone Di Mitri, Eugenio Ferrari, David Gauthier, Luca Giannessi, Giuseppe Penco, and Marco Veronese. New Scenarios of Microbunching Instability Control in Electron Linacs and Free Electron Lasers. In *8th International Particle Accelerator Conference*, 5 2017. doi: 10.18429/JACoW-IPAC2017-THYA1.

[55] Gianluca Geloni, Evgeni Saldin, Evgeni Schneidmiller, and Mikhail Yurkov. Transverse coherence properties of x-ray beams in third-generation synchrotron radiation sources. *Nuclear Instruments and Methods in Physics Research Section A: Accelerators, Spectrometers, Detectors and Associated Equipment*, 588(3):463–493, 2008. ISSN 0168-9002. doi: https://doi.org/10.1016/j.nima.2008.01.089.

[56] Y. T. Ding, Z. Huang, and S. A. Ocko. Transverse-Coherence Properties of the FEL at the LCLS. In *Proc. FEL'10*, pages 151–154. JACoW Publishing, Geneva, Switzerland, 2010.

[57] T Wodzinski, M Mehrjoo, M Ruiz-Lopez, B Keitel, M Kuhlmann, M Brachmanski, S Künzel, M Fajardo, and E Plönjes. Single-shot transverse coherence

measurements with young's double pinholes at FLASH2. *Journal of Physics Communications*, 4(7):075014, jul 2020. doi: 10.1088/2399-6528/aba3b0.

[58] Z. Huang, A. Brachmann, F.-J. Decker, Y. Ding, D. Dowell, P. Emma, J. Frisch, S. Gilevich, G. Hays, Ph. Hering, R. Iverson, H. Loos, A. Miahnahri, H.-D. Nuhn, D. Ratner, G. Stupakov, J. Turner, J. Welch, W. White, J. Wu, and D. Xiang. Measurements of the linac coherent light source laser heater and its impact on the x-ray free-electron laser performance. *Phys. Rev. ST Accel. Beams*, 13:020703, Feb 2010. doi: 10.1103/PhysRevSTAB.13.020703.

[59] C. Lechner et al. Demonstration of SASE Suppression Through a Seeded Microbunching Instability. In *Proc. FEL'14*, pages 177–180. JACoW Publishing, Geneva, Switzerland, 2014.

[60] E. Hemsing, G. Marcus, W. M. Fawley, R. W. Schoenlein, R. Coffee, G. Dakovski, J. Hastings, Z. Huang, D. Ratner, T. Raubenheimer, and G. Penn. Soft x-ray seeding studies for the slac linac coherent light source ii. *Phys. Rev. Accel. Beams*, 22:110701, Nov 2019. doi: 10.1103/PhysRevAccelBeams.22.110701.

[61] Haixiao Deng, Winfried Decking, and Bart Faatz. The echo-enabled harmonic generation options for FLASH II. *arXiv e-prints*, art. arXiv:1103.0112, March 2011.

[62] Primož Rebernik Ribič, Eléonore Roussel, Gregory Penn, Giovanni De Ninno, Luca Giannessi, Giuseppe Penco, and Enrico Allaria. Echo-enabled harmonic generation studies for the fermi free-electron laser. *Photonics*, 4(1), 2017. ISSN 2304-6732. doi: 10.3390/photonics4010019.

[63] Chao Feng, Haixiao Deng, Meng Zhang, Xingtao Wang, Si Chen, Tao Liu, Kaishang Zhou, Duan Gu, Zhen Wang, Zenggong Jiang, Xuan Li, Baoliang Wang, Wenyan Zhang, Taihe Lan, Lie Feng, Bo Liu, Qiang Gu, Yongbin Leng, Lixin Yin, Dong Wang, Zhentang Zhao, Guanglei Wang, and Dao Xiang. Coherent extreme ultraviolet free-electron laser with echo-enabled harmonic generation. *Phys. Rev. Accel. Beams*, 22:050703, May 2019. doi: 10.1103/PhysRevAccelBeams.22.050703.

[64] M. P. Dunning et al. A Proof-of-principle Echo-enabled Harmonic Generation FEL Experiment at SLAC. In *Proc. IPAC'10*, pages 2293–2295. JACoW Publishing, Geneva, Switzerland, 2010.

[65] Z T Zhao, D Wang, J H Chen, Z H Chen, H X Deng, J G Ding, C Feng, Q Gu, M M Huang, T H Lan, Y B Leng, D G Li, G Q Lin, B Liu, E Prat, X T Wang, Z S Wang, K R Ye, L Y Yu, H O Zhang, J Q Zhang, Me Zhang, Mi Zhang, T Zhang, S P Zhong, and Q G Zhou. First lasing of an echo-enabled harmonic

generation free-electron laser. *Nature Photonics Letters*, 6(May 2012):360–363, 2012. doi: 10.1038/NPHOTON.2012.105.

[66] C Evain, A Loulergue, A Nadji, J M Filhol, M E Couprie, and A A Zholents. Soft x-ray femtosecond coherent undulator radiation in a storage ring. *New Journal of Physics*, 14(2):023003, feb 2012. doi: 10.1088/1367-2630/14/2/023003.

[67] S. Thorin et al. Bunch Compression by Linearising Achromats for the MAX IV Injector. In *Proc. FEL'10*, pages 471–474. JACoW Publishing, Geneva, Switzerland, 2010.

[68] N. S. Mirian, G. Perosa, E. Hemsing, E. Allaria, L. Badano, P. Cinquegrana, M. B. Danailov, G. De Ninno, L. Giannessi, G. Penco, S. Spampinati, C. Spezzani, E. Roussel, P. R. Ribič, M. Trovó, M. Veronese, and S. Di Mitri. Characterization of soft x-ray echo-enabled harmonic generation free-electron laser pulses in the presence of incoherent electron beam energy modulations. *Phys. Rev. Accel. Beams*, 24:080702, Aug 2021. doi: 10.1103/PhysRevAccelBeams.24.080702.

[69] G Stupakov. Effect of finite pulse length and laser frequency chirp on hghg and eehg seeding. Technical report, SLAC National Accelerator Lab., Menlo Park, CA (United States), 11 2011.

Scientific publications

Author contributions

Paper I: Considerations on implementing EEHG with a strong linear chirp

M. Pop, F. Curbis, S. Werin, W. Qin
Proceedings of 39th Free Electron Laser Conference, 2019, pp. 262–265, Publisher: JACOW
The paper describes the effect a strong linear chirp in the electron beam has on the final phase space of a EEHG seeding technique. Through numerical simulations we showed that not only does the final bunching harmonic change but also the electron phase space changes drastically.

Contribution: I wrote the analysis software and developed the theory. I wrote the manuscript.

Paper II: A peak finding algorithm for FEL spectra characterization

M. Pop, E. Allaria, F. Curbis
Proceedings of 39th Free Electron Laser Conference, 2019, pp. 388–391, Publisher: JACOW
The paper illustrates the capabilities of a spectrum analysis tool developed in collaboration with FERMI. It highlights the information that can be extracted and shows correlations between different analysis parameters.

Contribution: I participated in developing the theory and wrote major part of the used simulation software. I participated in writing the manuscript.

Paper III: Single-shot transverse coherence in seeded and unseeded free-electron lasers: A comparison

M. Pop, E. Allaria, F. Curbis, et al.
Physical Review Accelerators and Beams, published 6th April 2022 DOI:10.1103/PhysRevAccelBeams.25.040
The paper characterizes the SASE and seeded FELs by their transverse coherence properties. Operating in both SASE and seeded mode on the same FEL, we were able to compare the different mechanisms underlying the development of transverse coherence in the two cases. The results, while in good agreement with existing theory clearly show that SASE and seeded FEL have different processes by which they become transversely coherent.

Contribution: I participated in the experiment, where I gathered and did initial analysis of the data. I did all the post experiment data analysis. I participated in developing the theory and in combining the existed theory with our experimental observations.

Paper IV: Mitigation of CSR induced spectral broadening in EEHG FEL

M. Pop, F. Curbis, S. Werin, E. Allaria
Manuscript
This work studies the effect of CSR on a general EEHG seeding scheme in terms of both the final bunching content and on the FEL radiation. Furthermore, a solution is proposed to mitigate this unwanted effect and to regain longitudinal coherence.

Contribution: I participated in developing the theory and conducted all the simulations. I participated in writing the manuscript and harmonizing our observations with existing theory.

Paper V: Analysis of the effect of energy chirp in implementing EEHG at SXL

M. Pop, F. Curbis, B.S. Kyle, S. Pirani, W. Qin S. Werin
Proceedings of the 12th International Particle Accelerator Conference, 2021 pp. 1566–1569, Publisher: JACOW

The work presented in this paper was done partly as a part of generating a CDR for the SXL project. I analyzed the possibility of seeding the soft X-ray FEL (SXL) with an EEHG technique incorporated in the last part of the final bunch compressor.

Contribution: I participated in developing the theory and conducted all the simulations. I wrote almost the entire manuscript.

Paper VI: Discussion on CSR instability in EEHG Simulation

D. Samoilenco, W. Hillert, F. Curbis, **M.Pop**, S. Werin, P. Niknejadi, G. Paraskaki and F. Panek
Proceedings of the 12th International Particle Accelerator Conference, 2021 pp. 1622–1625, Publisher: JACOW

The work presented in this paper was part of a broader collaboration between the universities of Hamburg and Lund called IFELD. The study concentrates on the CSR effect in the strong chicane of a EEHG seeding scheme on the final bunching wavelength.

Contribution: I participated in developing the theory and helped with the simulations. I participated in writing the manuscript.

Printed by Media-Tryck, Lund 2022 NORDIC SWAN ECOLABEL 3041 0903

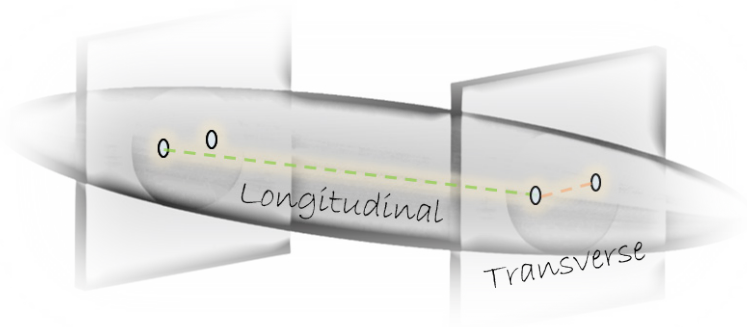

ISBN 978-91-8039-266-2
Division of Synchrotron Radiation Research
Department of Physics
Faculty of Science
Lund University